



**PEDRO MIGUEL MARTINS BOTELHO**  
BSc in ⟨Mechanical Engineering Sciences⟩

**CONTROL AND OPTIMIZATION OF  
DIMENSIONS AND CLEARANCES OF  
HIGH-PRESSURE COMPRESSOR BLADES OF  
THE LEAP-1A ENGINE**

DISSERTATION FOR THE DEGREE OF MASTER IN MECHANICAL  
ENGINEERING

MASTER IN MECHANICAL ENGINEERING  
NOVA University Lisbon  
⟨february⟩, ⟨2025⟩



# CONTROL AND OPTIMIZATION OF DIMENSIONS AND CLEARANCES OF HIGH-PRESSURE COMPRESSOR BLADES OF THE LEAP-1A ENGINE

DISSERTATION FOR THE DEGREE OF MASTER IN MECHANICAL ENGINEERING

**PEDRO MIGUEL MARTINS BOTELHO**  
BSc in (Mechanical Engineering Sciences)

**Adviser:** João Fradinho  
*Assistant Professor, NOVA University Lisbon*

# **Control and Optimization of Dimensions and Clearances of High-Pressure Compressor Blades of the LEAP-1A Engine**

Copyright © Pedro Miguel Martins Botelho, NOVA School of Science and Technology, NOVA University Lisbon.

The NOVA School of Science and Technology and the NOVA University Lisbon have the right, perpetual and without geographical boundaries, to file and publish this dissertation through printed copies reproduced on paper or on digital form, or by any other means known or that may be invented, and to disseminate through scientific repositories and admit its copying and distribution for non-commercial, educational or research purposes, as long as credit is given to the author and editor.

# Contents

<b>List of Figures</b>	<b>v</b>
<b>List of Tables</b>	<b>viii</b>
<b>Acronyms</b>	<b>xi</b>
<b>1 Introduction</b>	<b>1</b>
1.1 Motivation . . . . .	1
1.2 Objectives . . . . .	2
<b>2 Company and LEAP-1A Overview</b>	<b>3</b>
2.1 TAP M&E . . . . .	3
2.2 LEAP Engine . . . . .	4
2.2.1 Turbofan . . . . .	4
2.2.2 LEAP Family . . . . .	6
2.2.3 LEAP-1A . . . . .	7
<b>3 Compressor</b>	<b>12</b>
3.1 Axial Compressor . . . . .	12
3.2 Blisks vs Bladed disks . . . . .	14
3.3 Rotor Blades . . . . .	15
3.4 Degradation Mechanisms of Compressor Blades . . . . .	17
<b>4 Dimensional Inspection and Measurement Equipment</b>	<b>19</b>
4.1 Available Measurement Equipment . . . . .	19
4.1.1 Creaform HandySCAN 3D scanner . . . . .	19
4.1.2 Mitutoyo Euro-C 121210 . . . . .	20
4.2 TAP ME: Previous Theses on Dimensional Inspection . . . . .	22
<b>5 Problem Definition and Scope</b>	<b>23</b>
5.1 Blade Assembly Process and Clearance Requirements . . . . .	23

5.1.1	Defining Platform Tolerances and Tolerance Analysis Model for the Blade . . . . .	26
5.1.2	Analysis of Measurement Equipment Accuracy for Geometric Validation . . . . .	29
5.1.3	Spool Measurements and Specifications . . . . .	30
5.1.4	Contact Point Analysis Between Blades . . . . .	31
<b>6</b>	<b>Scan, Point Cloud Processing, and CAD Model</b>	<b>37</b>
6.1	Scanning Process of the Compressor Blade . . . . .	37
6.2	Point Cloud Processing and CAD Model Creation . . . . .	42
<b>7</b>	<b>Design and Application of Tooling for CMM: Fixation System Modeling</b>	<b>44</b>
7.1	Past Work . . . . .	44
7.2	Fixture Design . . . . .	45
7.2.1	6th and 7th Stage Blade Geometry Assessment . . . . .	45
7.2.2	Blade Fastening System . . . . .	45
7.2.3	Blade Spacing . . . . .	47
7.2.4	Fixture Threading and Transportation Features . . . . .	47
7.2.5	Fastening Feature of the Fixture with CMM's TTable . . . . .	47
<b>8</b>	<b>Tool Design for Blade Clearance Control</b>	<b>48</b>
8.1	Statistical Analysis for Tolerance Estimation . . . . .	48
8.1.1	Sampling Strategy . . . . .	48
8.1.2	Estimating Process Tolerance . . . . .	50
8.1.3	Conversion from Chord to Arc . . . . .	52
8.1.4	Spool diameter Tolerancing . . . . .	53
8.2	Tool Design . . . . .	54
8.2.1	Material . . . . .	55
8.3	Design Considerations . . . . .	55
8.4	Prototype Manufacturing . . . . .	58
<b>Bibliography</b>		<b>60</b>
<b>Appendices</b>		
<b>A Appendix</b>		<b>62</b>

# List of Figures

2.1	TurboJet Engine Work Cycle stages.[7]	4
2.2	Turbofan Engine. [1]	6
2.3	Leading Edge Aviation Propulsion (LEAP) Family.[2]	6
2.4	LEAP-1A.[2]	7
2.5	LEAP-1A Major Modules.[6]	8
2.6	LEAP-1A fan blades vs CFM56 fan blades.[12]	8
2.7	High and Low pressure rotors [12]	10
2.8	Low Pressure Turbine (LPT). [12]	10
2.9	Axial Compressor vs Turbine flow [18]	11
2.10	LEAP-1A Accessory Drives.[12]	11
3.1	Specific Consumption.[7]	12
3.2	LEAP-1A HPC.[12]	13
3.3	Axial Compressor Diagram and Pressure/Velocity Distribution.[7]	14
3.4	LEAP-1A HPC. [12]	15
3.5	Axial Fixing on the left and circumferential on the right.[7]	16
3.6	Stage 6 Blade Dimension Check.[12]	17
3.7	The effect on erosion trough time on the leading edge of a compressor blade [16]	18
3.8	Comparison of thrust-specific fuel consumption (TSFC) between eroded and new compressor blades.[16]	18
4.1	Mitutoyo Euro-C 121210 Components [16]	21
4.2	DOF of the Renishaw probe [15]	21
5.1	LEAP-1A High Pressure Compressor (HPC).	24
5.2	Stage Components and Clearance Representation	25
5.3	Stage Components and Clearance Representation	30
5.4	Contact zones identified by surface wear.	31
5.5	Contact zones identified by surface wear.	32

5.6	Contact zones identified by surface wear. . . . .	32
5.7	Contact zones identified by surface wear. . . . .	34
5.8	Contact zones identified by surface wear. . . . .	34
6.1	Initial scanning setup with fixed table and stationary blade. . . . .	37
6.2	Initial two blade positions used for scanning with the fixed table configuration. . . . .	38
6.3	Missing surface area in the sixth stage blade scan. . . . .	39
6.4	Final scanning setup with rotative table and integrated targets. . . . .	40
6.5	Final three blade positions used in the revised scanning approach. . . . .	40
6.6	Irregularities in the leading and trailing edges of the scanned mesh caused by limited point density. . . . .	41
6.7	Stage 6 Point Cloud . . . . .	41
6.8	Mesh and CAD Comparison . . . . .	42
6.9	Mesh and CAD Comparison . . . . .	42
7.1	Overlay of dovetail profiles from the 6th stage and 7th stage blades. . . . .	45
7.2	Exploded view of the fixture showing the base plate, bottom support block, top contact block, and clamping element. The geometry of the contact surfaces is adapted to the blade's platform and dovetail profile. . . . .	46
7.3	Contact surfaces on the blade that interface with the top contact block of the fixture. . . . .	46
7.4	Contact surfaces on the top contact block of the fixture, matching the geometry of the blade. . . . .	47
8.1	Platform blade with the chord dimension being measured, indicated as "x". . . . .	49
8.2	Schematic representation of the dovetail geometry and its key dimensions (A, B, C, D). . . . .	56
8.3	Functional tolerance window for the total blade chord length, based on spool perimeter limits adjusted by clearance allowances and arc-to-chord transformation. . . . .	57
8.4	First Tool Design. . . . .	58
A.1	Profile Measurement Report Blade 1 . . . . .	62
A.2	Profile Measurement Report Blade 2 . . . . .	63
A.3	Profile Measurement Report Blade 3 . . . . .	64
A.4	Profile Measurement Report Blade 4 . . . . .	65
A.5	Profile Measurement Report Blade 5 . . . . .	66
A.6	Profile Measurement Report Blade 6 . . . . .	67
A.7	Profile Measurement Report Blade 7 . . . . .	68
A.8	Profile Measurement Report Blade 8 . . . . .	69
A.9	Profile Measurement Report Blade 9 . . . . .	70
A.10	Profile Measurement Report Blade 10 . . . . .	71

A.11 First Tool Version 2D Drawing . . . . .	72
----------------------------------------------	----

## List of Tables

2.1	Transportes Aéreos Portugueses (TAP) Air Fleet Composition [3] . . . . .	3
2.2	Characteristics of the LEAP-1A engine.[4] . . . . .	7
2.3	Number of blades per stage on HPC [12] . . . . .	9
4.1	Renishaw probes available at TAP . . . . .	20
5.1	Assembly clearance tolerances for different stages. . . . .	25
5.2	Number of wide and narrow blades per stage. . . . .	27
5.3	Computed clearance values per stage. . . . .	28
5.4	Computed clearance values per stage using total interchangeability. . . . .	29
5.5	Diameter values for each stage . . . . .	31
5.6	CMM measured radii at left and right profiles for Narrow and Wide Body blades. . . . .	35
5.7	Summary of average and variation between maximum and minimum CMM-measured radii. . . . .	35
5.8	Estimated angles of the contact profiles within the YZ plane (in degrees). .	35
8.1	Pilot measurements of platform chord lengths (mm) for stages 6 to 10. . . . .	49
8.2	Calculated sample sizes for Narrow Body blades based on standard deviation from pilot sample, confidence level, and maximum error. . . . .	50
8.3	Calculated sample sizes for Wide Body blades based on standard deviation from pilot sample, confidence level, and maximum error. . . . .	50
8.4	Sample mean and tolerance estimates for each stage of the Narrow Body blades. . . . .	51
8.5	Sample mean and tolerance estimates for each stage of the Wide body blades.	51
8.6	Number of Wide, Narrow, and Lock Blades per Stage . . . . .	52
8.7	Total dimensional variation per stage . . . . .	52
8.8	Chord and Tolerance for Each Stage (Wide and Narrow) . . . . .	53
8.9	Spool measurements for engines 418 and 463 . . . . .	53
8.10	Nominal spool diameters and assumed manufacturing tolerance (IT3) . . .	54

8.11 Dovetail dimensions across different stages . . . . .	56
8.12 Admissible limits for the total blade chord length per stage . . . . .	58



## Acronyms

<b>CAD</b>	Computer-Aided Design 20
<b>CFMI</b>	CFM International 3
<b>CL</b>	Chord Length 21
<b>CMM</b>	Coordinate Measuring Machine 1, 20, 21, 29
<b>FOD</b>	Foreign Object Damage 17
<b>HP</b>	High Pressure 5, 9
<b>HPC</b>	High Pressure Compressor v, 1, 9, 12–15, 18, 20, 23, 24, 50
<b>HPT</b>	High Pressure Turbine 9
<b>LEAP</b>	Leading Edge Aviation Propulsion v, viii, 1, 3, 4, 6–8, 12–16, 24
<b>LET</b>	Leading Edge Thickness 21
<b>LP</b>	Low Pressure 5, 7–10
<b>LPC</b>	Low Pressure Compressor 8, 9, 13
<b>LPT</b>	Low Pressure Turbine v, 9, 10, 54
<b>ME</b>	Maintenance and Engineering 3, 19, 22, 25
<b>MM</b>	Major Module 9
<b>MRO</b>	Maintenance, Repair, and Overhaul 3
<b>RTM</b>	Resin Transfer Molding 8
<b>SB</b>	Service Bulletin 1
<b>TAP</b>	Transportes Aéreos Portugueses viii, 1, 3, 6, 19, 22, 25, 30, 37, 50
<b>TET</b>	Trailing Edge Thickness 21



# Introduction

## 1.1 Motivation

In 2016, CFMI launched the LEAP-1A engine, ushering in a new era of efficiency and performance for commercial aviation. This engine builds on the solid foundation laid by the CFM56, which has been one of the most trusted and widely used engines in the industry.

Over the course of its life, an engine undergoes numerous upgrades and refinements aimed at improving its performance and fuel efficiency. These improvements often focus on precise measurements and dimensional control, as well as maintenance standards that ensure the engine continues to run smoothly and reliably. By implementing these updates, the engine can perform at its best throughout its service life, maximizing efficiency and reducing operational costs. Additionally, these advancements are aligned with the growing need for more sustainable aviation technologies, helping to meet the industry's environmental goals.

Each time an engine manufacturer introduces an optimization, it is implemented through a [Service Bulletin \(SB\)](#), a document that communicates details of modifications that can be made to the aircraft.

In recent years, two students, Edgar Farinhas and Pedro Rendas, explored a method for measuring the rotor blade dimensions of the [HPC](#) using a [Coordinate Measuring Machine \(CMM\)](#) machine, focusing specifically on the blades of the CFM56 [HPC](#). [5]

Since it entered service, [TAP](#) has integrated the [LEAP-1A](#) into approximately half of its fleet, replacing the [CFM56](#). As the performance of the [HPC](#) directly influences engine efficiency and overall operational effectiveness, establishing robust monitoring and control measures has become a critical priority, alongside investigating the factors that affect its performance.

## 1.2 Objectives

Various factors influence engine performance, and the high-pressure compressor (HPC) plays a key role in this. The efficiency of the HPC is largely determined by the design of its rotor blades, which operate under intense aerodynamic and thermal conditions. This directly impacts the engine's performance and fuel consumption. Despite their importance, TAP has no standardized dimensional inspection process for these components.

Using the available equipment at the TAP Engine Shop, including the 3D scanner and Coordinate Measuring Machine (CMM), this study aims to develop a practical and efficient method for measuring the chord length of HPC blades, as this parameter is crucial in assessing blade wear and its correlation with engine performance in test cell conditions. Additionally, the study seeks to create a tool to measure the total clearance of the entire stage after assembly, optimizing the assembly process and making it more efficient.

An important objective is to control the platform gap of the blades during their preparation for assembly, developing a tool capable of accurately simulating the blade fit. This will enable the immediate determination of the required number of wide and narrow platform blades, making the process faster and more efficient—an important consideration for TAP's operational needs.

By establishing this methodology, it will be possible to correlate these geometric characteristics with engine performance as tested in the test cell. Understanding these relationships will help optimize maintenance procedures and improve overall efficiency. This thesis represents an important step toward implementing a more advanced dimensional inspection process at TAP, contributing to the company's ongoing efforts to enhance engine performance and reliability.

## Company and LEAP-1A Overview

### 2.1 TAP M&E

**TAP** was founded in 1945, during the end of World War II, a period marked by significant development in the aviation industry.

**TAP Maintenance and Engineering (ME)** is responsible for performing maintenance and engineering support services to **TAP**'s airline fleet and third-party customers. Services such as Aircraft Maintenance, Engine Repair and Overhaul and Components Repair and Overhaul.

To maintain **TAP** Air Portugal's reputation as one of the most reliable airlines in the world, **TAP ME** embraces the concept of *Care2Quality*. This philosophy is founded on three key pillars: **Safety**, **Quality**, and **Relationships**. It is integrated across all **TAP ME** products and services, which are organized into five main departments: *Care2Airframe*, *Care2Engines*, *Care2Components*, *Care2Engineering*, and *Care2Technical Labs*.

**TAP ME** offers extensive **Maintenance, Repair, and Overhaul (MRO)** services for a variety of aircraft systems and engine models. For **CFM International (CFMI)** engines, including the CFM56 series and **LEAP-1A**, it provides light and heavy maintenance, engine testing, troubleshooting, redelivery checks, technical consulting, and engine trend monitoring.

Currently in its fleet **TAP** has the following aircraft:

Table 2.1: **TAP** Air Fleet Composition [3]

Aircraft	Active N°	Age
Airbus A319ceo	3	23
Airbus A320ceo	15	19
Airbus A320neo	15	3
Airbus A321ceo	3	22
Airbus A321neo	12	4
Airbus A321LRneo	11	3
Airbus A330ceo	3	16
Airbus A330neo	19	5

## 2.2 LEAP Engine

LEAP engine family, developed and produced by CFM International—a joint venture between Safran Aircraft Engines and GE Aerospace—continues the legacy of the CFM56 as a best-seller in commercial aviation. Introduced in 2016, the LEAP powers the Airbus A320neo, Boeing 737 MAX, and COMAC C919, delivering a 15% improvement in fuel efficiency, along with reduced noise and emissions, while maintaining industry-leading reliability and cost-effectiveness. This advanced engine reflects the enduring success of the partnership between Safran and GE, which has been extended until 2050.

The LEAP, like most modern commercial aircraft engines, is a turbofan engine.

### 2.2.1 Turbofan

The Turbofan engine applies the same principle as the turbojet and all jet engines, Newton's third law: "For every action, there is an equal and opposite reaction". In this case, the first object is the engine itself and the second is the atmospheric air that is forced to accelerate as it passes through the engine causing the airplane to move forward.

To understand how the turbofan engine works, it is a good approach to analyze the turbojet working cycle and how it is processed first. As shown in Figure 2.1 the working cycle of a TurboJet has 4 main stages: Air intake, Compression, Combustion and Exhaust. At intake, the air is at atmospheric pressure, but as it passes through the compressors, it is compressed to optimal pressure and temperature conditions for combustion. Upon entering the combustion chamber, fuel nozzles mix the fuel and air, creating a homogeneous mixture that minimizes the peak temperature during combustion. During the combustion process, this mixture burns at constant pressure, increasing the air's volume while causing a decrease in pressure. The gases resulting from combustion expand through the turbine and jet pipe back to atmosphere providing the force needed to propel the airplane forward. During this part of the cycle, some of the energy in the expanding gases is turned into mechanical power by the turbine.

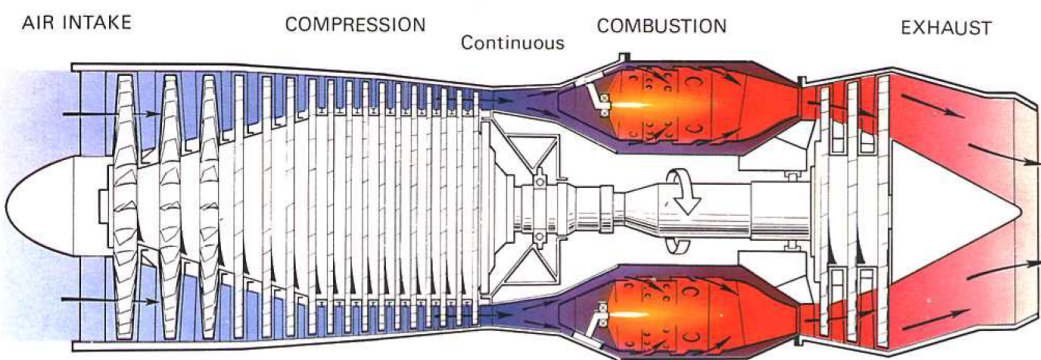


Figure 2.1: TurboJet Engine Work Cycle stages.[7]

Analysing the Turbofan work cycle requires a more complex approach since the air that goes through the combustor is now only responsible for 20% of the thrust power.

At the start, the engine's high-pressure shaft receives mechanical power with the assistance of a system called the Air Turbine Starter. This rotation drives the compressor blades, drawing air through the engine and initiating the compression process. The airflow through the engine also causes the fan to start moving. Once the engine reaches 20% of its maximum RPM, sufficient compression is generated to initiate combustion. With everything in motion, the engine enters a cycle similar to the turbojet working cycle. The gases produced from combustion expand through the **High Pressure (HP)** and **Low Pressure (LP)** turbines, delivering mechanical power to the **HP** and **LP** shafts. These shafts, in turn, transmit rotational energy to the **HP** and **LP** compressors as well as the front fan. As the fan rotates at high speed, it separates the incoming air into two distinct streams, forming the bypass ratio. Commercial aircraft engines, such as the LEAP-1A, are high-bypass ratio engines. In these engines, one stream of air enters the engine core, powering the turbojet-like working cycle. The remaining air, approximately 80% of the total intake, is channeled around the engine core. This bypassed air is directed into a narrow passage known as the fan duct, where its speed increases significantly. This accelerated airflow generates the majority of the thrust required to lift the aircraft.

In summary, the main differences between turbofan and turbojet engines lie in their airflow management and structural design. A key distinction is the large fan at the front of the turbofan, which directs a significant portion of the air around the engine core, defining the bypass ratio, which is the ratio of the amount of air bypassing the core to the amount of air passing through it, as illustrated in Figure 2.2. Weight wise, for the same power output, given the fact that all the high pressure rotating assemblies diameter can be reduced, the turbofan engines are lighter, improving the power-weight ratio of the engine. A low bypass ratio engine has a weight reduction of 20 percent compared to a pure jet engine for the same air mass flow.<sup>[7]</sup> Another significant advancement in turbofan engines is the introduction of the multi-spool or multi-shaft system, although this technology can also be applied to pure jet engines. The presence of both **LP** and **HP** turbines and compressors requires each assembly to rotate at different speeds, since just a percentage of the air that flows through the **LP** Compressor goes into the **HP** one (the majority of the air forms the bypass flow). This is essential for achieving higher efficiency, as each component operates at its optimal rotational velocity. Most commercial aircraft engines are high-bypass engines, and the typical configuration for these engines is a two-shaft system. As illustrated in Figure 2.2 the **LP** compressor is powered by a shaft coming from the **LP** turbine, and the same applies to the **HP** spool.

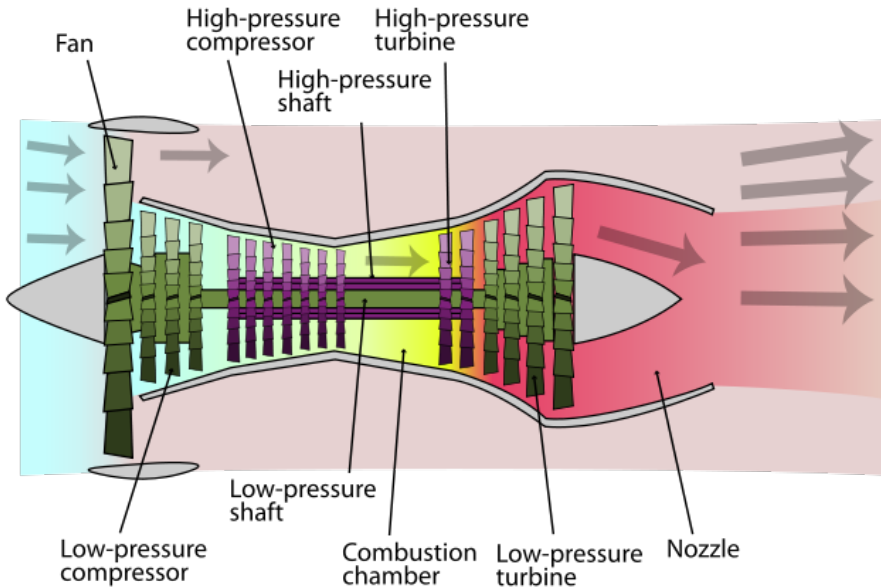


Figure 2.2: Turbofan Engine. [1]

### 2.2.2 LEAP Family

As mentioned at the beginning of this chapter, the LEAP engine powers a variety of aircraft, with its characteristics varying depending on the application. Therefore, we can categorize the LEAP engine family based on application and thrust power.

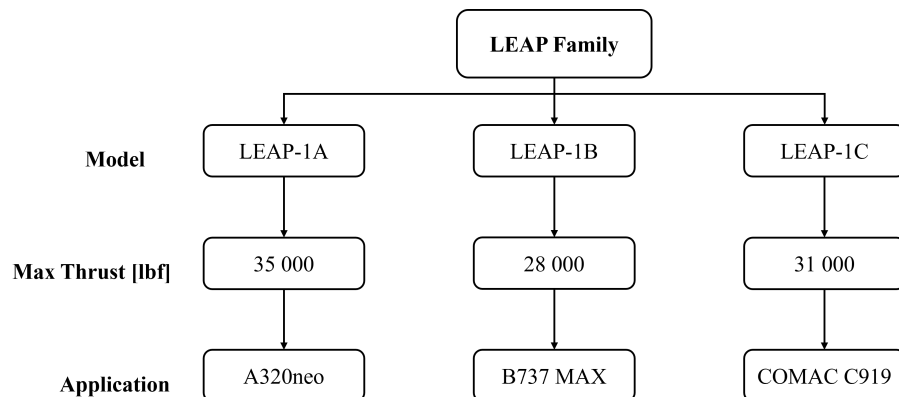


Figure 2.3: LEAP Family.[2]

Each model also has variations based on its thrust. For instance, the LEAP-1A can be further subcategorized into LEAP-1A23, LEAP-1A24, LEAP-1A26, LEAP-1A30, LEAP-1A32, LEAP-1A33, and LEAP-1A35. Considering that in 'LEAP-1A24', the '24' indicates the engine's thrust capacity of 24 klbf.

Currently, in the TAP Air Fleet Composition, the LEAP-1A26 and LEAP-1A32 engines are used respectively in the Airbus A320neo and A321neo.

### 2.2.3 LEAP-1A

The LEAP-1A, represented in Figure 2.4, is a high-bypass turbofan engine designed to power the next-generation Airbus A320neo. This section presents some of its key features, along with its main modules and innovations in comparison to its predecessor, the CFM56. Most of this information is derived from the engine's brochure and training manual.



Figure 2.4: LEAP-1A.[2]

This powerplant is presented with the following characteristics in Table 2.2.

Table 2.2: Characteristics of the LEAP-1A engine.[4]

Characteristic	Value
Takeoff thrust	Up to 35,000 lbf
Bypass ratio	11:1
Overall pressure ratio	40:1
Fan diameter	1.98 m (78 in)
Compressor stages (fan/booster/HPC)	1 + 3 + 10
Turbine stages (HP/LP)	2 + 7
Weight	3007 kg
Length	3.35 m (11 ft)
Width	2.53 m (8.3 ft)
Height	2.38 m (7.8 ft)

Design and function wise LEAP-1A present in its composition 4 Major modules. As represented in Figure 2.5, Fan and Booster, Core, LP Turbine and Accessory Drive Major Modules.

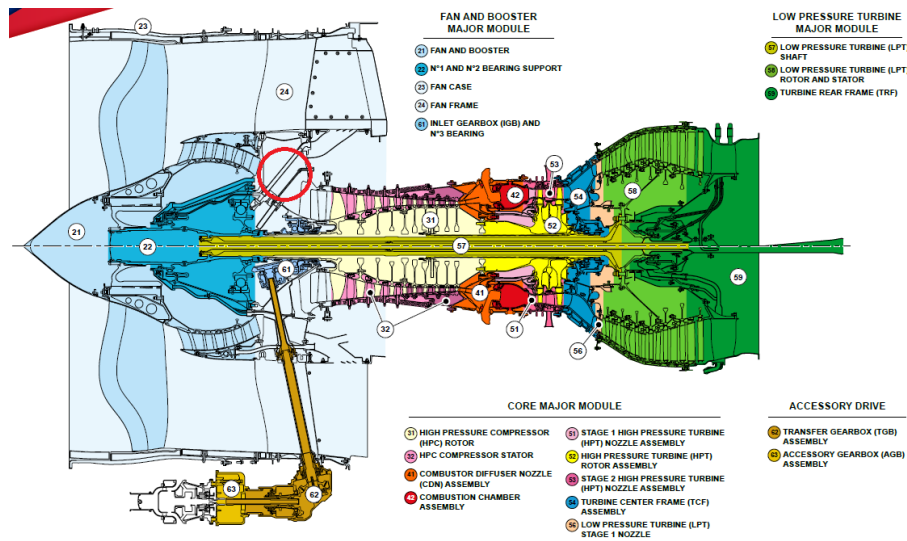


Figure 2.5: LEAP-1A Major Modules.[6]

### 2.2.3.1 Fan and Booster Major Module

As shown in Figure 2.5, the Fan and Booster Major Module consists of the Fan and Booster itself, two bearing supports, the fan case, the fan frame, the inlet gearbox, and the number 3 bearing.

The Fan and Booster assembly represents the integration of the front fan and the [LP Compressor](#).

The fan itself is composed of a single assembly that includes one front spinner, 18 fan blades, a flow splitter, and a platform front shroud.

The [Low Pressure Compressor \(LPC\)](#) consists of three stages: the first stage has 62 blades, the second stage has 75 blades, and the third stage has 72 blades.

One of the major technological breakthroughs in the new LEAP-1A engine is the production of its fan blades. These blades are manufactured using additive manufacturing with 3D-woven [Resin Transfer Molding \(RTM\)](#) carbon fiber composites. Compared to the solid titanium blades of the CFM56, this advancement allows for larger blades, as illustrated in Figure 2.6, without increasing the engine's weight. According to the company, this material helps reduce engine weight by 500 lbs per unit.

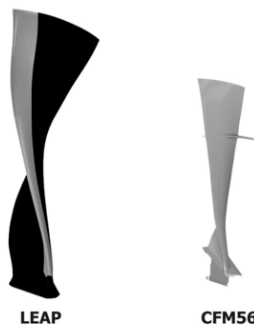


Figure 2.6: LEAP-1A fan blades vs CFM56 fan blades.[12]

In summary, the purpose of this engine assembly is to impart kinetic energy to the incoming airflow, separate the primary and secondary airflow, and expel the hot air generated by the engine.

### 2.2.3.2 Core

Next is the Core Major Module, which is responsible for generating thrust by producing power through highly compressed air.

This **Major Module (MM)** comprises the assembly of the **HPC**, combustion chamber, and **High Pressure Turbine (HPT)**. Additionally, it is divided into nine sub-modules.

The **HPC** consists of the HPC rotor and stator, while the **HPT** includes the HPT rotor along with the stage 1 and stage 2 nozzle assemblies. The Core Major Module also incorporates the Turbine Center Frame and the **LPT Stage 1 Nozzle**.

To achieve optimal performance, the **HPC** features 10 stages, as shown in Table 2.3. Each stage consists of one rotor and one stator. The first five stages of compression are achieved through blisks, while the remaining five stages use compressor blades with circumferential assembly. This mini module has the purpose of increasing the pressure of the booster discharge air for combustion.

Table 2.3: Number of blades per stage on HPC [12]

Stage	1	2	3	4	5	6	7	8	9	10
Number of blades	-	-	-	-	-	62+2+2	57+2+2	63+2+2	60+2+2	64+2+2

It is important to note that the HPC rotor is coupled with the HPT, as shown in Figure 2.7. This coupling allows the kinetic energy extracted from the HPT to be used for compressing the airflow. Likewise, the same principle applies to the **LPC** and **LPT**.

In Figure 2.7, the yellow assembly represents the Low-Pressure rotor, while the orange assembly corresponds to the High-Pressure rotor.

As mentioned in 2.2.1, these rotors rotate at different speeds. The **LP** rotor operates at N1 speed (3 850 RPM), whereas the **HP** rotor rotates at N2 speed (16 645 RPM).

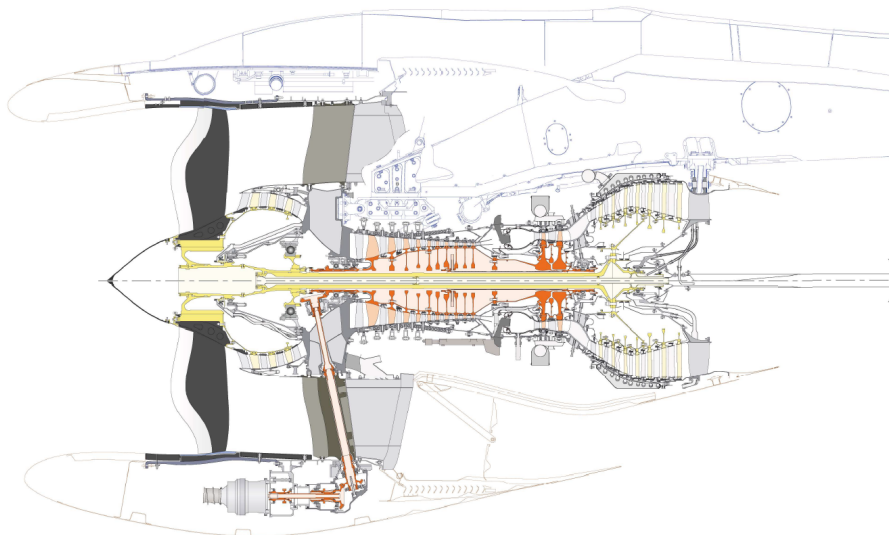


Figure 2.7: High and Low pressure rotors [12]

### 2.2.3.3 LP Turbine Major Module

The LP Turbine Major Module, represented in Figure 2.8, is composed by the LP turbine shaft, rotor and stator and the turbine rear frame.

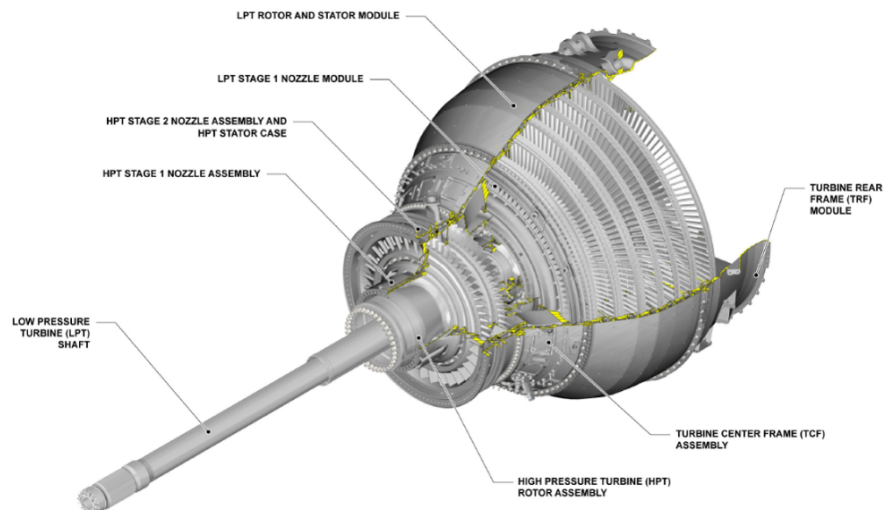


Figure 2.8: LPT. [12]

Its primary function is to supply mechanical power to the LP Compressor by converting the thermal energy from the hot gases released from the combustion chambers into kinetic energy while simultaneously decompressing it.

It is worth noting that while both turbines and compressors present similar designs and compositions, their functions are fundamentally opposite.

As previously mentioned, compressors consume energy and transfer it to the air, compressing it while increasing its velocity, whereas turbines absorb energy from the expansion of the combustion gases and convert it into mechanical power.

Both components consist of stages that include one stationary and one rotating element, but their purposes and arrangements differ. As illustrated in Figure 2.9, in a compressor, a rotor row is followed by a stationary vane row, while in a turbine, a stationary nozzle precedes a rotating rotor row. The stationary vanes in the compressor are responsible for further compressing the air through diffusion processes, whereas the nozzles in the turbine decompress the airflow and guide it in the most efficient direction, maximizing the kinetic energy absorbed by the turbine blades.

A more detailed explanation of the compressor's operation is provided in the following sections.

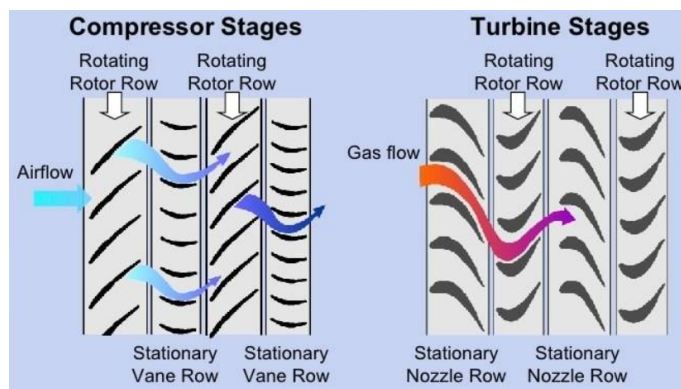


Figure 2.9: Axial Compressor vs Turbine flow [18]

#### 2.2.3.4 Accessory Drive

As shown in Figure 2.10, the accessory drive delivers torque to the HPC to initiate engine start-up, as described in 2.2.1, enabling the compression process (red arrow path). During the engine's operating cycle, it supplies mechanical energy to both the aircraft and engine accessories (orange arrow path).

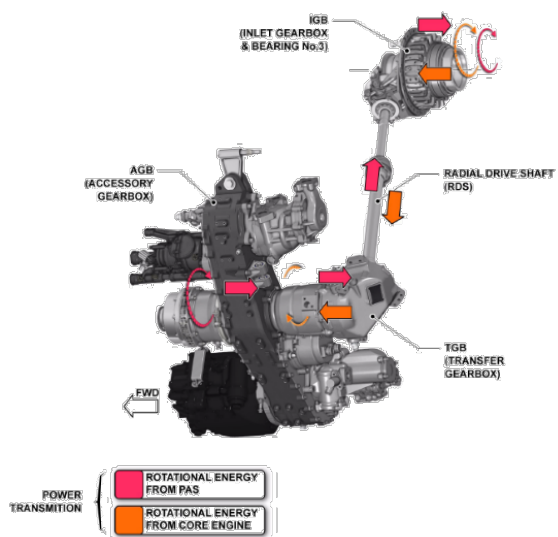


Figure 2.10: LEAP-1A Accessory Drives.[12]

# Compressor

Being the purpose of this thesis "*Control and Optimization of High-Pressure Compressor Blade Dimensions and Clearances,*" it is crucial to study the operation of engine compressors, understanding their working principles and the key criteria that must be considered in order to improve the blades dimensions and clearances in engine reliability and performance.

This section highlights the key criteria, provides an overview of the module's operation, and explains how compressor wear during the engine's operating cycle affects its performance.

## 3.1 Axial Compressor

In gas turbine engines, there are two primary types of compressors: axial and centrifugal flow compressors. Both are driven by a shaft connected to the turbine; however, the axial type is easier to manufacture and can be designed to achieve higher pressure ratios. For this reason, commercial turbofan engines typically utilize this type of compressor, specifically in the [LEAP-1A](#) engine.

Higher pressure ratios are proven to improve fuel consumption as shown on Figure 3.1

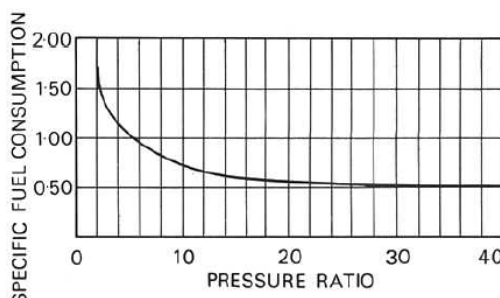


Figure 3.1: Specific Consumption.[\[7\]](#)

Using the [LEAP-1A HPC](#) as example, an axial compressor consists of one or more rotor assemblies which in turn can be one single part, representing a blisk, or a circumferential

### 3.1. AXIAL COMPRESSOR

blade assembly. These assemblies are mounted between the 2 bearing in a casing which incorporate the stator vanes.

As mentioned in the previous sections, this compressor is a twin-spool, multi-stage unit consisting of 3+10 stages.

In other words, the compressor is composed of the [LPC](#) with three stages, followed by the [HPC](#) with ten stages. Additionally, the front fan can also be considered part of the compression system, as it contributes to air compression despite not being its primary function, effectively serving as the first stage of the [LPC](#).

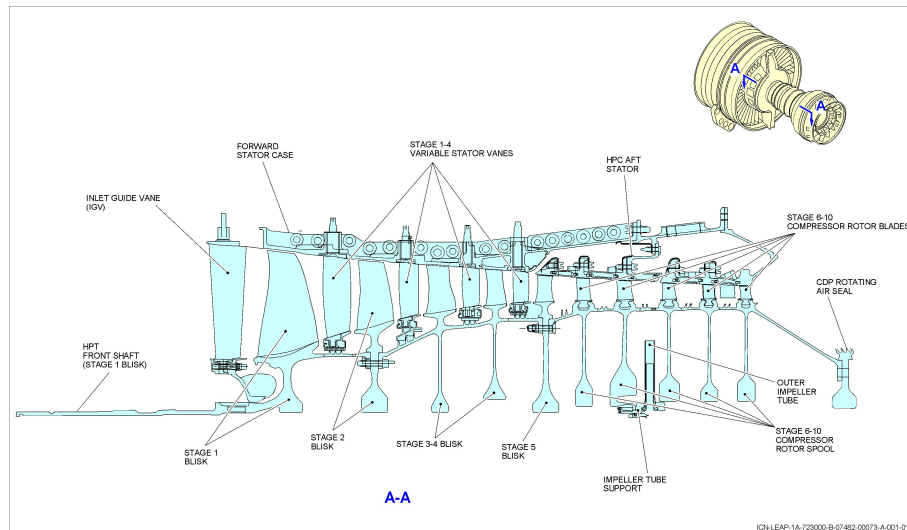


Figure 3.2: LEAP-1A HPC.[\[12\]](#)

With the engine running, the turbine transmits power to the compressor, driving it at high speed and ensuring a continuous airflow. As the air enters the [LPC](#), it passes through the first rotor, where the rotating airfoil-shaped blades transfer kinetic energy to the airflow by increasing its tangential momentum. Simultaneously, pressure rises with the aid of the diffusion process. Next the air flows into the vanes where kinetic energy increase is converted in pressure increase by the same process found in the rotational step.

The requirement for a high-pressure ratio on the shaft demands precise airflow control during engine operation to prevent airflow reversal, as a compressor inherently forces air from a low-pressure region to a higher-pressure zone. To achieve this, the guide vanes in the initial four stages functions as Variable Stator Vanes (VSV's), followed by fixed stator vanes in the subsequent stages. These variable vanes progressively close at lower airflow speeds to maintain an optimal air angle on the downstream rotor blades, preventing reverse flow and avoiding compressor stall.

During each stage the increase of pressure is relatively small as shown in Figure 3.3 in order to avoid air breakaway at the blades and subsequent blade stall. On another hand, the multi-stage process allows the [LEAP](#) to achieve an Overall Pressure ratio of 40:1. This ratio represents the Pressure ratio of all the engine not just the compressor.

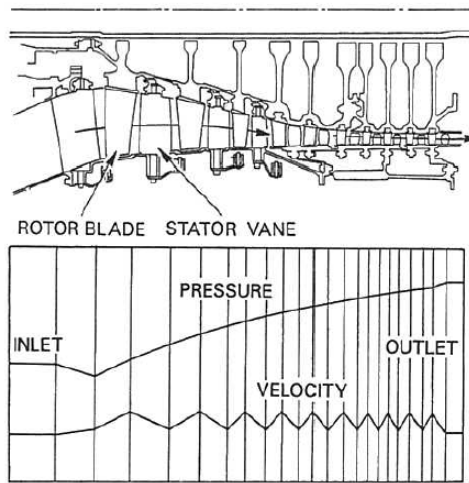


Figure 3.3: Axial Compressor Diagram and Pressure/Velocity Distribution.[\[7\]](#)

### 3.2 Blisks vs Bladed disks

In Figure 3.4, the HPC of the LEAP-1A engine is shown, consisting of five blisks, an impeller tube support, a five-stage rotor, and a rotating seal.

The incorporation of blisks in compressors represents a significant innovation in the LEAP-1A design compared to previous-generation turbofan engines. This advancement was introduced in aviation to enhance engine performance. Blisks significantly reduce rotor weight compared to conventional aero-engine disks. Since compressor and turbine disks contribute to over 20% of the engine's structural weight, their design presents numerous static and dynamic challenges.

From a design perspective, traditional bladed disks require the assembly of multiple components with different connection features, such as airfoil roots, disk roots, and locking mechanisms. In contrast, a blisk integrates all these elements into a single part, leading to several benefits:

- A reduction in the total number of parts, contributing to lower overall weight and faster assembly.
- Fewer contact surfaces, minimizing gaps where airflow could infiltrate and disrupt engine operation.
- Eliminates dovetails and its associated issues such as its weight and propensity for leakages.
- Simplified assembly during both production and maintenance, resulting in lower manufacturing costs and shorter lead times.

- The use of blisks imply bigger clearance between the blade tip and the stator which impacts engines performance.

However, blisks present significant drawbacks when compared to bladed disks, particularly in terms of maintenance and repairability. In the event of damage to an individual airfoil, the entire blisk must be replaced, leading to considerably higher costs than replacing a single blade. Additionally, as a single integrated component, the blisk eliminates the option of using different materials for the airfoil and the disk. The increased rigidity of the blisk also results in a lack of damping, which reduces its fatigue resistance.

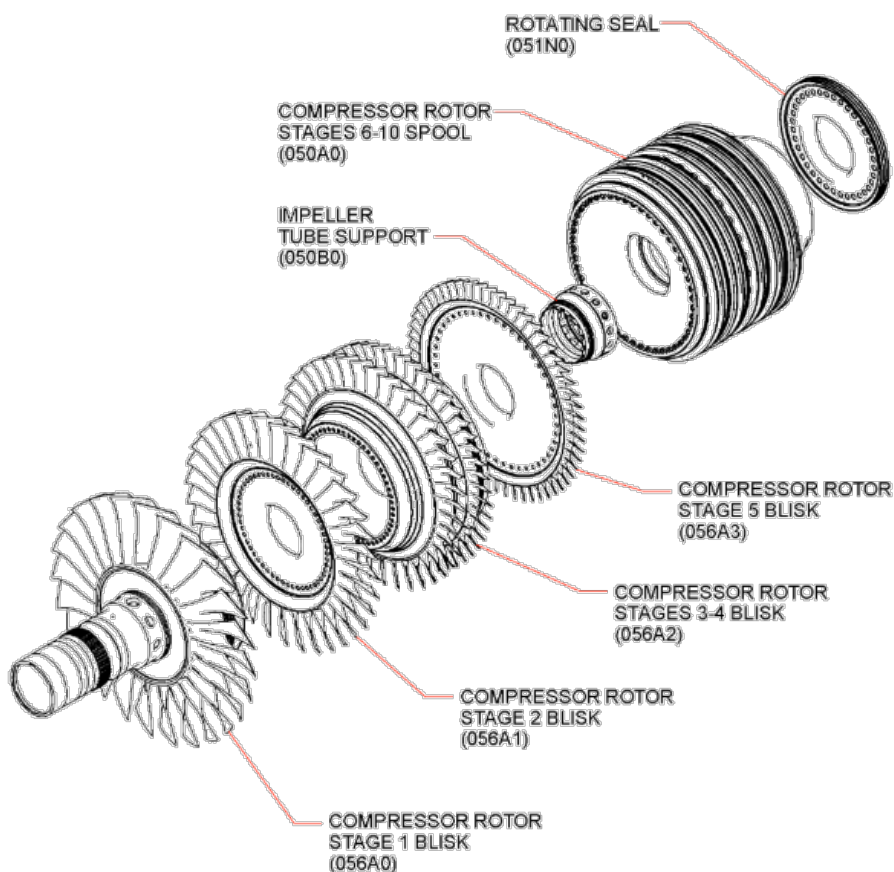


Figure 3.4: LEAP-1A HPC. [12]

### 3.3 Rotor Blades

As previously described, the **HPC** of the **LEAP-1A** consists of 10 stages, with the first five rotors designed as blisks and the last five as disks with fixed rotor blades. The attachment of these blades to the disk can be achieved through two different methods: axial or circumferential fixing, as illustrated in Figure 3.5.

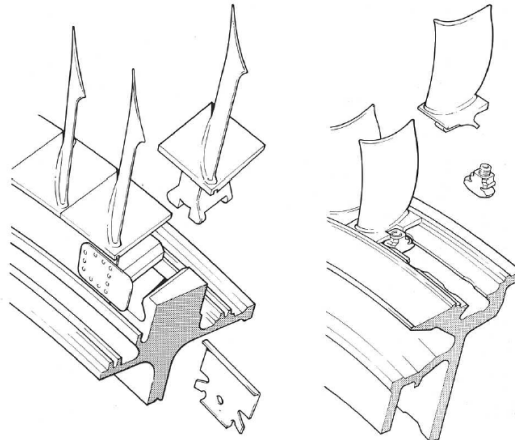


Figure 3.5: Axial Fixing on the left and circumferential on the right.[7]

The blades and disk shown in Figure 3.5 are not actual LEAP-1A components but merely illustrative examples.

The blades of the last five stages of the HPC are made from Inconel 718 and Inconel 718Plus. Inconel 718 is used in the first two stages, while Inconel 718Plus is used in stages 8, 9, and 10.

This material differs from the the blades found on the LPC or the blisks since with the increase of pressure temperature also rises.

INCONEL alloy 718 (UNS N07718/W.Nr. 2.4668) is a high-strength, corrosion-resistant nickel chromium material used at -252.78 to 704.44°C. [10]

Focusing on the last five stages of the HPC, in alignment with the objectives of this thesis, it is crucial to understand which dimensions impact the engine's performance, particularly as blade dimensions undergo changes due to excessive wear and usage, ultimately affecting engine performance and reliability.

TAP ME technicians are responsible for monitoring the most critical dimensions during the engine repair process.

These dimensions are specified in [12] and are illustrated in Figure 3.6. Based on this, the critical dimensions can be defined as follows: tip chord length (CH), blade tip length (H), leading edge thickness (TL), and trailing edge thickness (TU).

### 3.4. DEGRADATION MECHANISMS OF COMPRESSOR BLADES

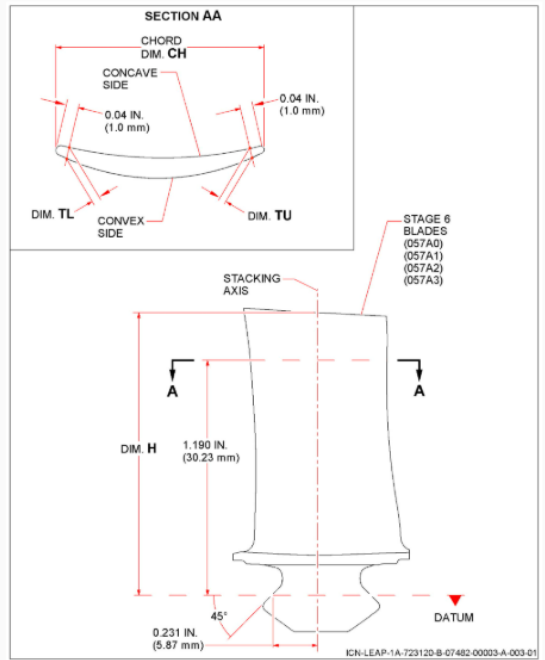


Figure 3.6: Stage 6 Blade Dimension Check.[\[12\]](#)

In each stage of the HPC, the blades can be categorized into three types: narrow body blades, wide body blades, and locking blades. The narrow and wide body blades are used to adjust the platform gaps, ensuring proper assembly and optimal aerodynamic performance. The locking blades, on the other hand, incorporate locking mechanisms that secure them in place, preventing movement during engine operation. The correct selection and placement of these blade types are essential to maintaining structural integrity and performance within the compressor. Therefore, ensuring the correct gap between the blades during the repair process is crucial to maintaining proper assembly, aerodynamic efficiency, and overall engine reliability.

## 3.4 Degradation Mechanisms of Compressor Blades

The degradation of compressor blades is a critical factor affecting engine performance and reliability. Commercial aircraft engines operate in diverse environments, exposing the engine core to various particles and contaminants.

These ingested particles, collectively known as **Foreign Object Damage (FOD)**, include sand, metal fragments, birds, and other debris. The ingestion of such contaminants has two main consequences: if the particle is a hardbody, it can cause direct erosion and structural damage to the blades, leading to dimensional loss. In contrast, if the particle is a softbody, such as a bird, it can obstruct airflow, causing performance degradation or even severe engine failure.

In particular, this section examines the impacts of FOD on the geometry of compressor blades. The ingestion of particles during the engine cycle can lead to a reduction in

blade chord, loss of blade thickness, alteration of the leading and trailing edge shapes, thinning of the blade trailing edge, blunting of the leading edge, and an increase in surface roughness.

Alterations in the blade geometry, such as changes in chord length, thickness loss, and alterations to the leading and trailing edges, result in increased clearance losses at the blade tips, higher frictional losses, and a significant reduction in off-idle and open beta stall margins. In Figure 3.7 its possible to observe the damages caused on the leading edge by continuous erosion. [16]

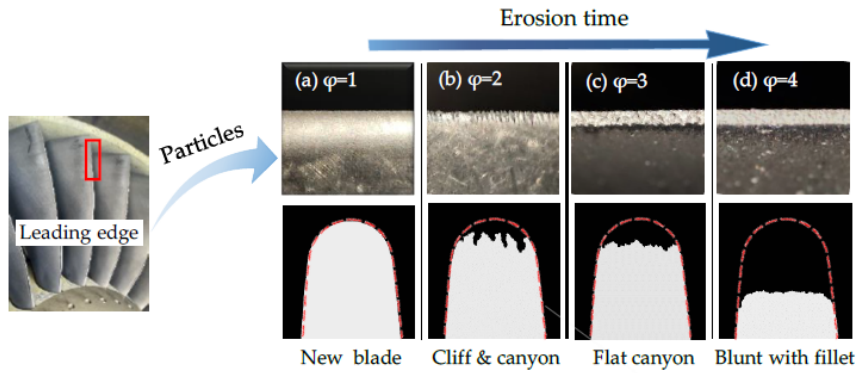


Figure 3.7: The effect on erosion trough time on the leading edge of a compressor blade [16]

These effects influence HPC efficiency and, consequently, engine performance. In particular, compressor blade erosion, coupled with efficiency losses throughout the engine, can increase fuel consumption by nearly 1 percent compared to new blades (see Figure 3.8) [16].

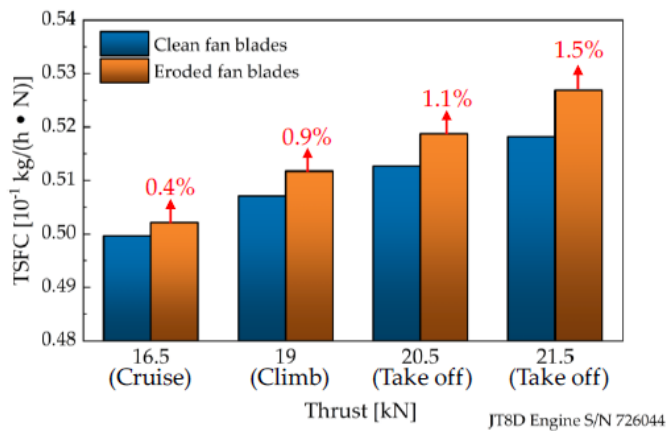


Figure 3.8: Comparison of thrust-specific fuel consumption (TSFC) between eroded and new compressor blades.[16]

# Dimensional Inspection and Measurement Equipment

This chapter introduces the equipment and methodology that can be used for dimensional inspection in engine component analysis. Keeping parts within the required tolerances is essential for ensuring performance and durability. A 3D scanner makes it possible to generate a digital model of the components, while a coordinate measuring machine (CMM) allows for precise measurement and comparison with nominal dimensions. These tools help improve the accuracy of the analysis and support potential optimization of the components at [TAP ME](#) Engine Shop.

The Engine Shop at [TAP ME](#) has a specialized Dimensional Inspection department responsible for verifying component dimensions in accordance with the manual, ensuring optimal engine performance and reliability.

## 4.1 Available Measurement Equipment

To ensure precise measurements, the department relies on advanced equipment, such as the Creaform HandySCAN 3D scanner, which captures highly accurate digital models of components, and the Mitutoyo Euro-C 121210 coordinate measuring machine (CMM), which provides detailed dimensional and geometric analysis. By using these tools, the team can carry out thorough inspections, verify tolerances, and explore opportunities for improving component performance.

### 4.1.1 Creaform HandySCAN 3D scanner

The HandySCAN 3D is a high-precision laser scanner developed by Creaform, designed for portable 3D scanning of objects with complex geometries. It uses laser triangulation to capture detailed 3D models with high accuracy and resolution. It presents the following technical data:

- **Accuracy:** 0.025 mm (0.0009 in)

- **Volumetric Accuracy:** Up to 0.020 mm + 0.015 mm/m
- **Light Source:** 22–30 blue laser lines
- **Working Distance:** 200 to 750 mm
- **Recommended Part Size Range:** 0.05 – 4 m
- **Weight:** 0.94 kg

The HandySCAN 3D laser scanner is used in conjunction with VXelements, an integrated 3D software platform that allows real-time data acquisition, post-processing, and analysis.

During the development of this thesis, this equipment will enable the practice of reverse engineering. Using the HandySCAN 3D scanner, detailed physical data from the HPC blades can be captured, and with the VXelements software, the point cloud is transformed into a 3D Computer-Aided Design (CAD) model. This model can then be imported into SolidWorks for further analysis and used to design the workpiece, which will be employed in the CMM to securely hold the blades during measurement.

#### 4.1.2 Mitutoyo Euro-C 121210

The CMM is a highly precise tool used to measure the geometry of parts and components. It works by using a probe that senses the physical contact with the object. While traditional CMMs rely on touch-trigger probes, there are other models that use laser or optical sensors to take measurements. The Mitutoyo Euro-C 121210 CMM is controlled by a computer and operates within a three-dimensional coordinate system.

This particular CMM is equipped with a Renishaw Revo-2, providing it with five degrees of freedom (DoF). In addition to moving along the three main axes, the machine can adjust the probe's angles, enabling it to measure even the most complex surfaces that would otherwise be difficult to reach. The machine setup includes a granite bed, probe, probe tree, arm, joystick, and specialized software, as shown in Figure 4.1.

Although four probes are available for use with the Renishaw Revo-2, only two are applicable to this project. Among them, the RSP2-3 is the sole probe that enables full five-degree-of-freedom operation. As illustrated in Figure 4.2, the first three DoFs (X, Y, and Z) are controlled by the CMM arm, while the remaining two ( $\alpha$ ,  $\beta$ ) are executed by the probe itself.

Each probe has distinct characteristics suited for different tasks, as detailed in Table 4.1.

Table 4.1: Renishaw probes available at TAP

Probe	DoF	Scanning Capability	Sphere Ø
RSP2-3	5	2D	6mm
RSP3	3	3D	4mm

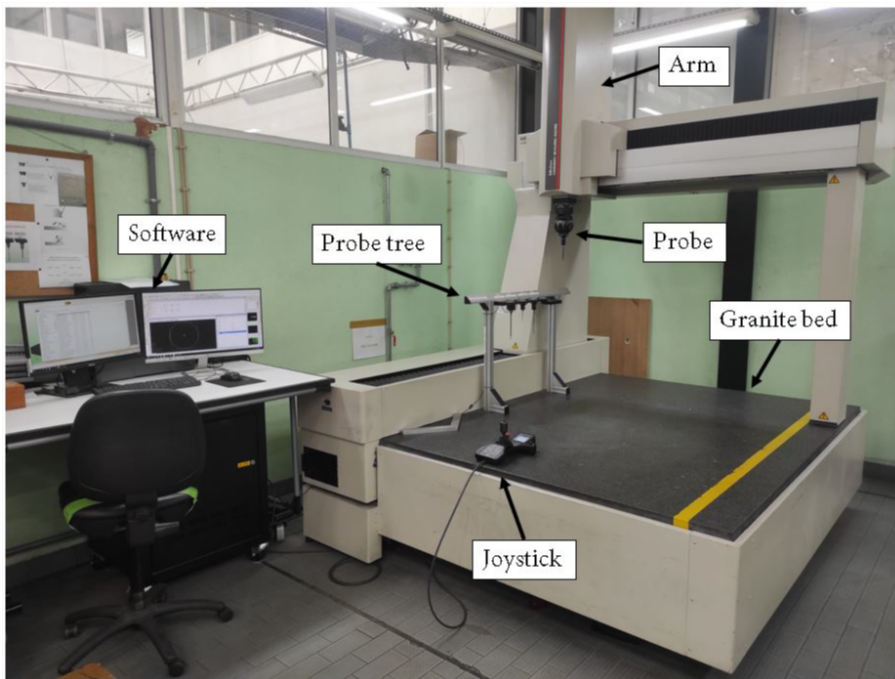


Figure 4.1: Mitutoyo Euro-C 121210 Components [16]

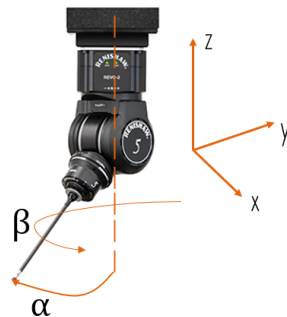


Figure 4.2: DOF of the Renishaw probe [15]

The integration of the CMM into this project plays a key role in ensuring that every high-pressure compressor rotor blade is measured quickly, accurately, and consistently. The development of a custom inspection program aims to enable the production team to measure entire sets of blades with minimal manual intervention, enhancing both efficiency and reliability.

Through the use of the CMM, it is possible to automatically verify critical dimensions, such as Chord Length (CL), Leading Edge Thickness (LET), Trailing Edge Thickness (TET), and overall airfoil geometry. This ensures that each blade meets the required tolerances while eliminating inconsistencies associated with manual measurement methods. Additionally, this automation reduces the workload of operators, allowing them to focus on other essential tasks while the machine performs the measurements.

Another significant advantage of the CMM is its ability to generate detailed inspection

reports, facilitating the tracking of blade conditions over time. This capability extends beyond simple compliance verification, contributing to predictive maintenance strategies that enhance engine performance and reduce unexpected maintenance costs.

By incorporating this level of automation and precision into the inspection process, the proposed approach aims to streamline production, improve quality control, and establish a more efficient and standardized methodology for [TAP](#)'s maintenance operations.

## 4.2 TAP ME: Previous Theses on Dimensional Inspection

In the past, several master's theses have been developed in collaboration with [TAP ME](#), contributing to the improvement of measurement and inspection processes for aircraft engine components. One of these studies was conducted by Farinha, E. [5], focusing on the design of a fixture and the development of a measurement method for high-pressure compressor (HPC) rotor blades. This research continued the work initiated by Rendas, P. [13], who laid the foundation for the development of a fixture specifically designed for HPC rotor blade inspection.

Additionally, Baptista, F. [14] contributed to this field by developing a model that predicts the off-design performance of the CFM56-5B turbofan engine. More recently, Guerreiro, A. [8] worked on the development of a process to measure the exit flow area of the low-pressure turbine (LPT) nozzles from the same engine model. His study focused on creating an automated program for Coordinate Measuring Machine (CMM) inspection, addressing a previously undeveloped process within [TAP ME](#)'s engine maintenance operations.

While previous studies have primarily focused on components of the CFM56-5B engine, this thesis aims to extend the dimensional inspection process to the HPC rotor blades of the LEAP-1A engine. One project involves developing an optimized CMM measurement program for assessing the blade chord to evaluate performance, utilizing data from the test bank. The second project focuses on measuring and controlling platform clearance to optimize the assembly process. These improvements, applied to both the LEAP and CFM engines, build on previous research, further advancing the continuous optimization of inspection methods to adapt to newer engine generations.

# Problem Definition and Scope

This thesis tackles two key challenges in the assembly of HPC (High Pressure Compressor) blades. The goal is to ensure that the assembly process meets the required specifications and to better understand how blade geometry impacts engine performance.

The first challenge is to develop a process or tool that guarantees the correct assembly clearance for the blades. This clearance must comply with the specifications outlined in the engine manual, ensuring that the blades are assembled properly and function as intended.

The second objective is to create a reliable method for measuring the chord length of the blades and analyzing its correlation with engine performance in bench tests. By understanding this relationship, we can gain valuable insights into how small variations in manufacturing affect overall efficiency and explore ways to optimize the assembly process. Ultimately, this aims to guarantee and control engine performance according to operational needs.

Together, these objectives shape the scope of this work, which involves designing measurement tools, validating methodologies, and bridging the gap between manufacturing precision and engine performance.

In this chapter, the details of these challenges will be explored, along with the initial requirements and decisions that guided the approach taken. This will provide a comprehensive understanding of the context, constraints, and considerations that influenced the development of solutions throughout the project.

## 5.1 Blade Assembly Process and Clearance Requirements

This study focuses on the assembly of HPC stages 6 to 10, represented in Figure 5.1, as these are the stages that incorporate the blades under analysis, as previously mentioned. The assembly of **HPC** blades follows a standardized procedure to ensure precise positioning and compliance with the required specifications. The process begins with preparing the spool, where blade slots and wire seal grooves are cleaned and inspected. Contaminants are removed to ensure a smooth surface for blade insertion. Wire seals are then

installed in the grooves, adhering to specified clearance tolerances to maintain structural integrity.



Figure 5.1: LEAP-1A HPC.

The blades are then inserted into the spool, following a controlled sequence to ensure a uniform distribution. During this step, each blade is checked for free movement within the dovetail slot, as any restrictions may indicate the need for replacement. After all blades are in place, locking blades are installed in designated positions to secure the assembly.

To finalize the assembly, locking lugs are positioned and their set screws are torqued to the required values. A detailed verification is performed to ensure that the locking lugs are correctly engaged within the spool's dovetail lock slot, preventing unintended movement. To confirm the correct platform clearance, the blades are shifted in one direction to determine the maximum gap, and measurements are taken to verify compliance with the permissible range. This clearance, referred to as Clearance R, is represented in Figure 5.2. If necessary, adjustments are made by replacing narrow-platform blades with wide-platform ones.

## 5.1. BLADE ASSEMBLY PROCESS AND CLEARANCE REQUIREMENTS

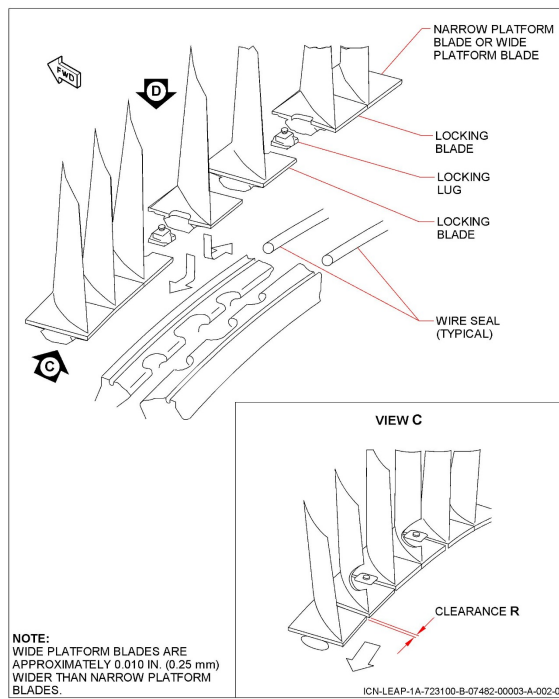


Figure 5.2: Stage Components and Clearance Representation

The measurement of the clearance is performed using a feeler gauge (with a corresponding image), ensuring precise determination of the gap. For each compressor stage, a predefined clearance value is specified, as presented in Table 5.1. In the aviation industry, these clearance values are typically provided in inches. However, throughout the development of this dissertation, all measurements have been converted to millimeters to maintain consistency.

Once the correct blade sequence and clearance are established, the assembly is re-installed, and a final torque check is performed on the locking lugs. Ensuring that all components remain within the prescribed limits is critical to maintaining engine performance and durability, as deviations from the specified tolerances can lead to excessive wear, unwanted vibrations, or mechanical failures.

Stage	Assembly Clearance Tolerance [in]	Assembly Clearance Tolerance [mm]	Clearance [mm]
6	0.010-0.030	0.254-0.762	
7	0.010-0.030	0.254-0.762	
8	0.010-0.030	0.254-0.762	0.508
9	0.080-0.100	2.032-2.54	
10	0.149-0.169	3.7846-4.2926	

Table 5.1: Assembly clearance tolerances for different stages.

Currently, in TAP's ME Engine Shop assembly process, there is no method to anticipate this clearance before the assembly stage. As a result, if the measured clearance after

assembly does not fall within the required specifications, additional wide-platform blades may need to be sourced from the supplier. This can introduce delays in the workflow, as the availability of the necessary blades depends on supplier lead times. As represented in Figure 5.2, wide-platform blades are approximately 0.25 mm wider than narrow blades, allowing for clearance adjustments when needed. Implementing a way to predict and control clearance earlier in the process would help streamline operations, reducing waiting times and improving overall efficiency.

As a first step, it is necessary to construct a nominal model of the blades from which further work can be carried out. This model will serve as the foundation for predicting and controlling assembly clearances, ensuring compliance with specifications, and improving process efficiency.

### 5.1.1 Defining Platform Tolerances and Tolerance Analysis Model for the Blade

One of the primary challenges in ensuring proper assembly clearance is the precision required to construct a nominal model of the blades. The assembly clearance depends on the individual blade dimensions, particularly the platform width, as these factors determine how the blades fit within the spool slots. To develop an effective process, it is essential to establish a nominal blade model with a precision level derived from the permissible clearance tolerances.

The required precision level can be derived from the assembly clearance by considering the maximum allowable variation that still maintains compliance. This ensures that the model reflects real-world manufacturing conditions and enables accurate clearance prediction.

To define the tolerance for the nominal model, a statistical approach is utilized, as described in [11]. Unlike the total interchangeability model, where tolerances are summed linearly, the statistical model considers the probability distribution of component variations. The assembly tolerance is calculated using the following equation:

$$T_{\text{conj}} = \sqrt{\sum_{i=1}^n t_i^2} \quad (5.1)$$

where:

- $T_{\text{conj}}$  - Assembly Tolerance
- $t_i$  - Part Tolerance

This approach reduces the overall tolerance accumulation, making it more suitable for large-scale production where component variations follow a normal distribution. By applying this model, it is possible to maintain a precise nominal blade model while accommodating natural manufacturing variations.

### 5.1.1.1 Calculation of Platform Dimensional Tolerance for Each Blade Type and Stage Using the statistical model

To evaluate the dimensional tolerance for each compressor stage, the number of wide and narrow blades assembled in the engine was analyzed. Table 5.2 presents the distribution of wide and narrow blades for each stage, along with the total number of blades. The assembly data was collected from a motor assembled in the workshop to determine the exact number of blades used.

Stage	Wide Blades	Narrow Blades	Total Blades
6	26	36	62
7	24	33	57
8	24	39	63
9	23	37	60
10	26	38	64

Table 5.2: Number of wide and narrow blades per stage.

Using the equation 5.1, and considering an assembly tolerance of 0.508 mm, we analyze the case for stage 6, which has 26 wide blades and 36 narrow blades. Being almost identical parts, its assumed that the wide body and narrow body blades present the same tolerance,  $T_w = T_n$ , the equation simplifies to:

$$T_{\text{conj}} = \sqrt{26T_w^2 + 36T_n^2} \quad (5.2)$$

$$T_{\text{conj}} = \sqrt{62T_w^2} = \sqrt{62}T_w \quad (5.3)$$

Since the total assembly tolerance is given as 0.508 mm:

$$0.508 = \sqrt{62}T_w \quad (5.4)$$

Solving for  $T_w$ :

$$T_w = \frac{0.508}{\sqrt{62}} = 0.0646 \text{ mm} \quad (5.5)$$

Thus, the tolerance for each blade in stage 6 is approximately \*\*0.0646 mm\*\*.

Based on this analysis, the clearance values were calculated. Table 5.1.1.1 presents the obtained results.

These calculations, derived from workshop data and statistical analysis, ensure that the clearance assessment aligns with real assembly conditions. Furthermore, they provide insight into the required precision needed to develop a nominal model that enables a feasible and applicable solution.

Stage	Clearance (mm)	$T_w = T_n$
6		0,0645
7		0,0673
8	0.508	0.0640
9		0,0656
10		0,0635

Table 5.3: Computed clearance values per stage.

### 5.1.1.2 Calculation of Platform Dimensional Tolerance for Each Blade Type and Stage Using the Total Interchangeability Model

To assess the dimensional tolerance for each compressor stage under the total interchangeability model, we assume that all blades—wide and narrow—must individually conform to the overall assembly tolerance. This approach does not take into account statistical variations and instead assumes that each blade directly contributes to the total variation without reduction factors. The total interchangeability model represents a worst-case scenario and serves as a reference to highlight its impracticality compared to statistical models.

Using the same distribution of wide and narrow blades from Table 5.2, we analyze the tolerance requirement for each stage. The total tolerance allocation assumes that each blade's tolerance adds directly to the overall variation, leading to a simplified summation approach:

$$T_{\text{conj}} = (26 + 36)T_w = 62T_w \quad (5.6)$$

Given that the total assembly tolerance remains at 0.508 mm:

$$0.508 = 62T_w \quad (5.7)$$

Solving for :

$$T_w = \frac{0.508}{62} = 0.00819 \text{ mm} \quad (5.8)$$

Thus, under the total interchangeability model, each blade in stage 6 would require an individual tolerance of approximately 0.00819 mm, which is significantly tighter than the 0.0646 mm derived from the statistical model.

Applying the same method to other stages yields the results presented in Table 5.4.

These results clearly indicate that the total interchangeability model imposes unrealistically strict tolerances on each blade, making it practically infeasible for manufacturing and assembly. This reinforces the necessity of using statistical models to optimize tolerance allocation while maintaining feasible manufacturing constraints.

Stage	Clearance (mm)	(Total Interchangeability)
6	0.508	0.00819
7	0.508	0.00891
8	0.508	0.00806
9	0.508	0.00847
10	0.508	0.00782

Table 5.4: Computed clearance values per stage using total interchangeability.

As such, in this work, the statistical model was chosen as the reference for tolerance calculations, as it provides a more realistic and achievable approach while ensuring the necessary precision for assembly.

### 5.1.2 Analysis of Measurement Equipment Accuracy for Geometric Validation

Following this analysis, the next steps involve evaluating the available equipment previously mentioned in 4, specifically the Creaform HandySCAN 3D scanner and the Mitutoyo Euro-C 121210 CMM. While the application of reverse engineering using the scanner enables the creation of a model, its lower accuracy on edges may compromise the precision required to resolve the problem. Therefore, it is necessary to use the CMM to obtain the geometry with the required accuracy. Additionally, the scanner enables the development of the CMM fixture, which will be designed using knowledge from previous dissertations.

The accuracy of the available equipment is as follows:

- HandyScan accuracy: 0.001 in (0.0254 mm)
- Peripheral tape accuracy: 0.0005 in (0.0127 mm)
- CMM accuracy: 0.00001 in (0.00000254 mm)

These values highlight the significant difference in measurement precision, reinforcing the need for a combined approach to achieve the required accuracy.

It is essential to follow the golden rule of metrology, known as George Berndt's law, which states that "the measurement uncertainty should not exceed 1/10 of the tolerance of the dimension being controlled." This principle ensures that the selected measurement tools provide results with a level of precision suitable for the given tolerances.

It is important to note that the CMM at TAP is currently inoperative (INOP), and during this project, TAP proceeded with the purchase of a new machine. However, to expedite the work, a machine was made available by the R&D department of Hanon Systems, which will allow progress in the project and facilitate the measurement of the platform profile of the blades to properly define the dimensions required for the work

Therefore, while the HandyScan may be useful for generating general models, the CMM will be the preferred equipment to ensure that the calculated tolerances, particularly values as small as 0.0646 mm (for stage 6), are met with precision. The combination of these tools will provide a robust and accurate approach to validating and controlling assembly tolerances, ensuring that the blades fit correctly and optimizing engine performance.

### 5.1.3 Spool Measurements and Specifications

To ensure precise assembly and proper clearance for the HPC blades, it is essential to define the key dimensions of the spool. The spool serves as the foundational structure for blade installation, and its dimensions directly impact the assembly process.

These dimensions play a crucial role in determining the fit and function of the HPC blades. The slot width and depth directly influence how securely the blades are held in place, while the groove width and depth are vital for the proper installation of wire seals. Additionally, platform clearance values dictate the permissible gap between adjacent blades, ensuring compliance with operational specifications.

The diameter measurements were obtained using a Peripheral tape on a previously used spool available on TAP's engine shop. During the measuring process it was possible to differentiate two different spool diameters per stage,  $\phi Up$  and  $\phi Down$ , represented in Figure 5.3. Having this two different diameters per stage implies that the blades do not rest on the spool over two equal diameters, resulting in a lack of symmetry between these two geometries. Table 5.5 presents the measured diameters. Later on section ?? this subject is studied in more depth.

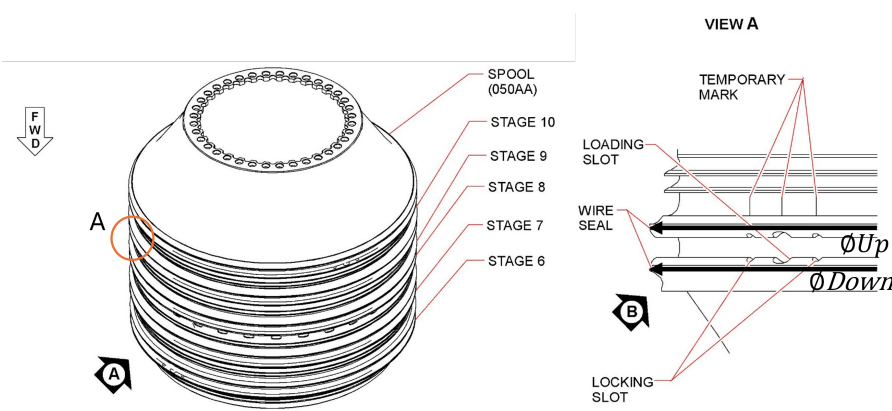


Figure 5.3: Stage Components and Clearance Representation

By integrating these spool measurements into the assembly process analysis, it is possible to predict and optimize the blade fitting conditions before final assembly, reducing rework and improving overall efficiency.

Stage	$\varnothing$ Up [in]	$\varnothing$ Down [in]	$\varnothing$ Up [mm]	$\varnothing$ Down [mm]
10	15.675	15.69	398.145	398.526
9	15.704	15.66	398.882	397.764
8	15.670	15.62	398.018	396.748
7	15.620	15.69	396.748	398.526
6	15.545	15.52	394.843	394.208

Table 5.5: Diameter values for each stage

#### 5.1.4 Contact Point Analysis Between Blades

This section aims to identify the exact regions where contact occurs between adjacent blade platforms. The 3D scans of the blades do not offer sufficient resolution to precisely capture the geometry and curvature of the contact surfaces. Therefore, a more detailed analysis is required in these specific areas to understand how the platforms interact and to accurately determine where contact takes place during assembly and operation. To better understand how these surfaces interact, a two-part analysis was carried out: first through visual inspection of used blades to identify real contact marks, and then through precise CMM measurements to characterise the geometry of the contact areas.

To improve the dimensional characterization of the contact area between adjacent blade platforms, two reference profiles were defined: the left profile and the right profile. This naming helps simplify and organize the analysis that follows, making it easier to distinguish the different contact zones being assessed. Figure 5.4 shows the selected profiles and their location on the blade geometry.

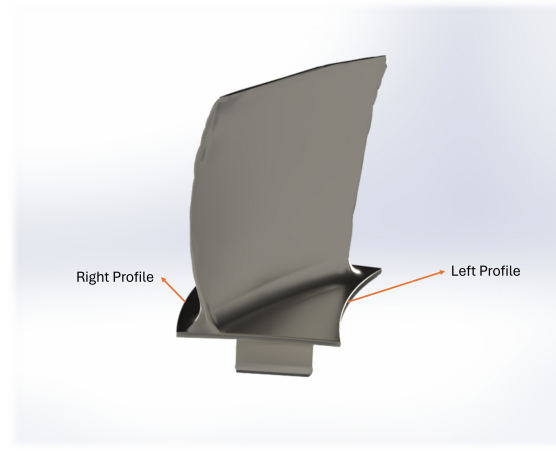


Figure 5.4: Contact zones identified by surface wear.

##### 5.1.4.1 Visual Inspection of Used Blades: Identifying Contact Zones

Initially, to understand where contact between adjacent blades occurs, five used narrow-body blades and five used wide-body blades were randomly selected from a worn LEAP-1A engine. Since these blades had already been in operation, the wear marks left by

contact made it possible to visually identify the contact zones. Evidence of contact was observed mainly at the extremities of both profiles, as shown in Figure 5.5.



Figure 5.5: Contact zones identified by surface wear.

As shown in Figure 5.6, this contact pattern consistently appears across all the selected blades, confirming the repeatability of the phenomenon.

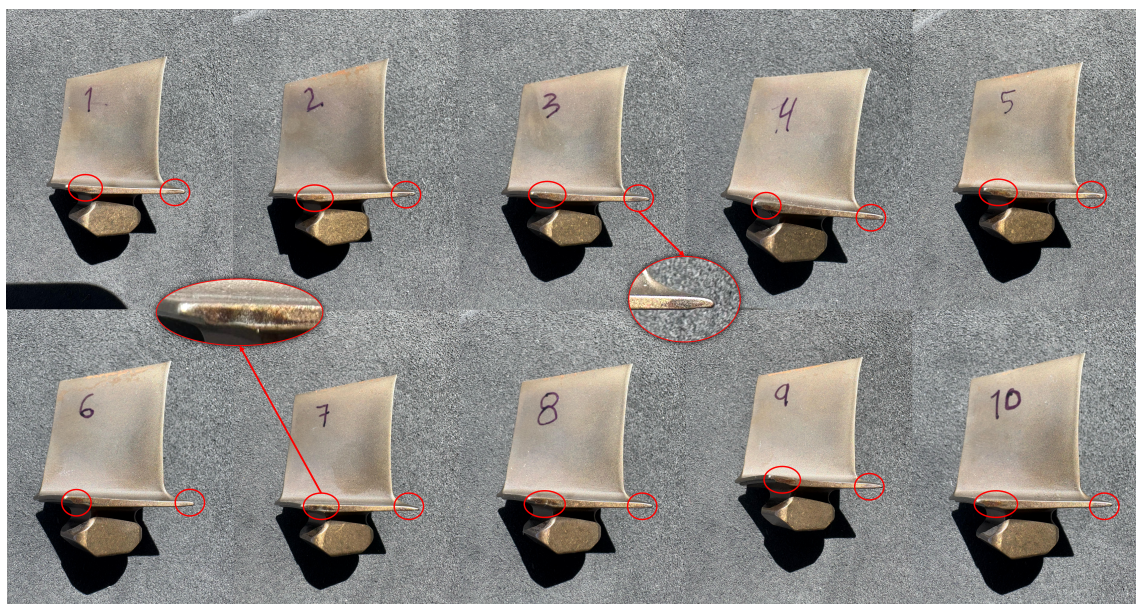


Figure 5.6: Contact zones identified by surface wear.

The presence of consistent wear marks at the extremities of both profiles suggests that these are the actual contact points during blade assembly. This indicates that the platform clearance is effectively defined at these specific regions, making them the critical areas to consider when trying to understand how the assembly gap is established in practice.

#### 5.1.4.2 Dimensional Characterization of Blade Contact Surfaces Using CMM

As established in Section 5.1.1, the dimensional tolerances required for blade manufacturing are extremely tight. For example, using the statistical tolerance model, the sixth stage of the HPC assembly demands a manufacturing tolerance of just **0.0645 mm** per blade. According to the metrology rule referred in 5.1.2, the measurement uncertainty

## 5.1. BLADE ASSEMBLY PROCESS AND CLEARANCE REQUIREMENTS

must be no greater than one-tenth of the tolerance. Therefore the required measurement uncertainty must be below **0.00645 mm (6.45 µm)**.

As previously discussed, the HandySCAN 3D scanner, although highly useful for general reverse engineering tasks, does not provide the necessary accuracy in critical areas such as blade edges or contact surfaces. Its resolution is insufficient to guarantee the precision needed for meaningful dimensional comparison at this scale.

For this reason, it became essential to resort to measurement by Coordinate Measuring Machine (CMM), which provides the required level of precision to properly define the problem dimensionally and allow for accurate blade analysis.

The CMM available at TAP ME normally offers a precision of 0.001 inches (25.4 µm). However, due to it being out of service at the time of this work, an alternative CMM was made available by the R&D department of Hanon Systems. This machine operates with a precision of **1.6 + L/350 µm**, where  $L$  is the length of the measured feature in millimetres.

For the measurements carried out on the contact profiles, this results in a measurement uncertainty of **1.6605 µm** for the left profile and **1.6614 µm** for the right profile—well within the required accuracy range for this analysis.

Before each measurement, the CMM performs an initial alignment process to establish the coordinate system (X, Y, and Z axes) and ensure that the fixation tool is correctly positioned. This procedure is illustrated in Figure 5.7, which shows the alignment sequence in three steps.

In the first step (left image), the probe detects four points on the base of the fixation tool to define the initial plane — the YX plane.

Next (middle and right images), the machine scans four points on each lateral side of the fixation tool, resulting in eight points in total. Based on these, it calculates an intermediate surface that defines the YZ plane.

Finally, a single point is probed on the front face of the fixation tool (right image), allowing the system to determine the XZ plane and complete the coordinate setup.

While this method ensures consistency in positioning, it also presents a limitation: the alignment is referenced to the fixation tool rather than the blade itself. As a result, slight geometric deviations between individual blades may go unnoticed, reducing the accuracy of contact surface comparisons.

In this analysis, the same ten randomly selected sixth stage blades previously examined for surface wear — five narrow-body and five wide-body — were measured to capture detailed geometric data from the contact zones and assess part-to-part variation.

The resulting coordinate system, defined through this alignment procedure, is represented in Figure 5.8, which was extracted from the CMM simulation software and visually illustrates the orientation of the X, Y, and Z axes relative to the fixture.

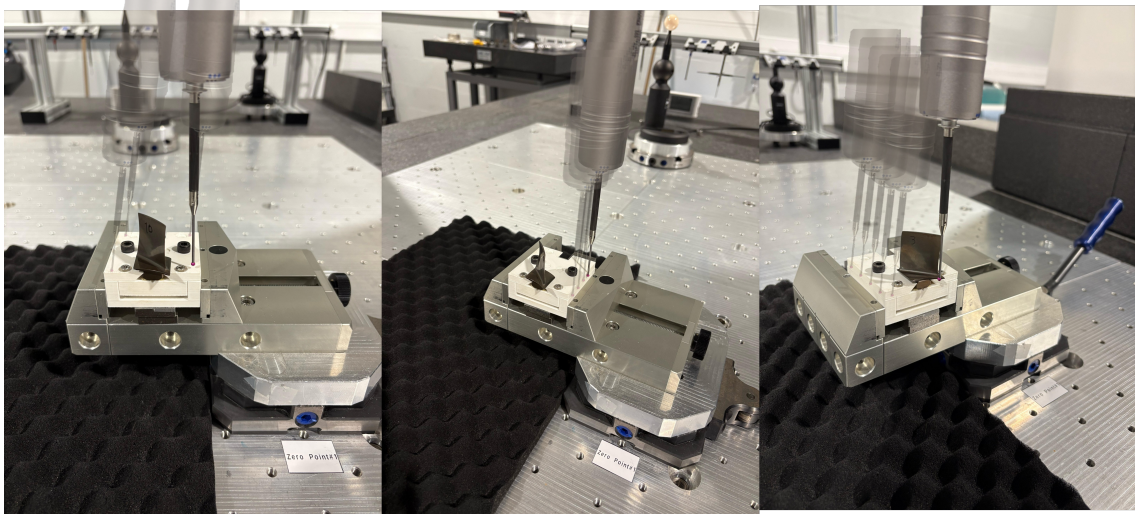


Figure 5.7: Contact zones identified by surface wear.

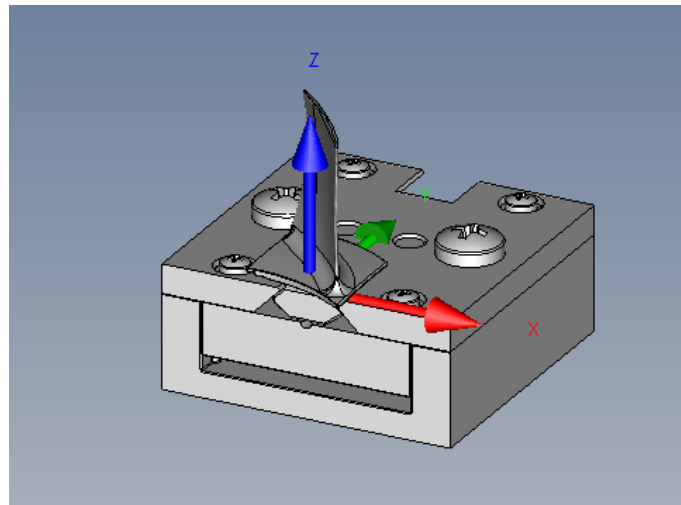


Figure 5.8: Contact zones identified by surface wear.

The CMM measurement procedure consisted of single passes along the contact profiles. For each blade, the probe performed three scan paths: one on the left profile and one on the right profile with 400 points each, and two additional passes on the left profile at different heights. These dense point clouds allowed for a detailed reconstruction of the contact surface geometry. Additionally, with the last two passes the system estimated the angle of the contact profile within the YZ plane to better understand the surface orientation. All individual measurements are presented in the annex, and the measured curvature radii are summarized in the following table.

## 5.1. BLADE ASSEMBLY PROCESS AND CLEARANCE REQUIREMENTS

---

Table 5.6: CMM measured radii at left and right profiles for Narrow and Wide Body blades.

Narrow Body Radius (mm)			Wide Body Radius (mm)		
Blade N°	Left Profile	Right Profile	Blade N°	Left Profile	Right Profile
1	30.7734	30.548	6	30.6168	30.6588
2	30.7584	30.545	7	30.5421	30.6623
3	30.7627	30.5403	8	30.5850	30.6342
4	30.7451	30.5411	9	30.5942	30.6323
5	30.7355	30.5327	10	30.6379	30.6614
<b>Avg</b> 30.7550		<b>Avg</b> 30.5414	<b>Avg</b> 30.5952		<b>Avg</b> 30.6498

Table 5.7: Summary of average and variation between maximum and minimum CMM-measured radii.

Profile	Narrow Body (mm)		Wide Body (mm)	
	Left	Right	Left	Right
Average Radius	30.7550	30.5414	30.5952	30.6498
Max-Min Variation	0.0379	0.0153	0.0958	0.0300

Based on the results presented in Table 5.7, the average values of the measured radii for each profile were defined as the nominal dimensions to be used in the blade model. The corresponding variations between the maximum and minimum values measured for each profile are considered representative of the dimensional tolerance associated with each nominal value. This approach ensures that the nominal model reflects the actual manufacturing variability observed across the sampled blades.

Additionally, as shown in the reports presented in the appendix and previously referenced, these measurements also aimed to estimate the angle of the contact profile within the YZ plane. However, due to the complex geometry and the limited thickness available for probing, the resulting values showed significant variation between blades. This results are presented in Table 5.8

Table 5.8: Estimated angles of the contact profiles within the YZ plane (in degrees).

Left Profile Angle (°)	Right Profile Angle (°)
-23.0719	-34.9658
-31.6433	-34.7307
-36.5751	-36.2302
-35.0147	-37.0324
-38.9593	-32.0996

These results are presented in Table 5.8, which highlights the lack of consistency between the measured angles. Given this high variability, it was concluded that these values cannot be reliably used to define a nominal model for the contact profile geometry. Therefore, angle estimation was excluded from the subsequent dimensional analysis.

In the following chapters, if angle measurement becomes necessary, the measurement procedure will need to be revisited. This may involve using different probe paths or adopting a more suitable strategy to capture the angular orientation of these narrow surfaces with greater repeatability.

# Scan, Point Cloud Processing, and CAD Model

## 6.1 Scanning Process of the Compressor Blade

The scanning of the compressor blade marked the initial phase of this work, aiming to generate a precise and detailed digital model of its complex geometry. The scanning process was designed to encompass all necessary surfaces while minimizing errors and distortions. Throughout this process, two main software tools were used: VXelements, for scan acquisition and initial alignment, and VXmodel, for advanced mesh editing and preparation for CAD reconstruction.

In the initial approach, a fixed table with pre-positioned targets was used, as shown in Figure 6.1, where the blade was placed and the operator moved around the part with the scanner, capturing different angles to ensure full surface coverage.

Setup  
initial

Figure 6.1: Initial scanning setup with fixed table and stationary blade.

A technician from the Dimensional Inspection department at [TAP](#) carried out the scan using the Creaform HandyScan, a handheld 3D scanner. The targets placed on the table served as reference points for the scanner's software, allowing it to maintain continuous alignment and improve the overall accuracy of the scanning process. For this acquisition, a resolution of 0.008 inches was selected, although the HandyScan is capable of reaching a resolution as fine as 0.004 inches, the chosen setting was deemed sufficient to accurately capture the blade's geometry without significantly increasing the scan duration or file size.

For this first approach, scanning was performed with the blade placed in two different positions, as shown in Figure 6.2

Pos. Pds

Inicial

Figure 6.2: Initial two blade positions used for scanning with the fixed table configuration.

The scanning process began by placing the blade in its first orientation on the fixed table with the targets already positioned. The scan was initiated in the VXelements software, and the operator proceeded to move the HandyScan 3D device manually around the blade, performing multiple passes to capture data from all visible surfaces. Throughout this stage, it was often necessary to adjust the scanner's shutter speed in order to improve fluidity, reduce interruptions, and optimize surface acquisition in areas with challenging reflectivity.

Once the scanning pass was complete, the acquisition was stopped both on the HandyScan device and within the software. At this point, an initial cleanup was performed: the scan was filtered to remove noise, eliminate unwanted data such as the table, the targets, or stray reflections, and retain only a clean point cloud of the blade. This initial scan was saved, and a visual assessment was made to identify any areas of the blade geometry that were still missing or insufficiently captured.

The blade was then repositioned to expose the previously hidden surfaces, and a new scanning session was started. The process was repeated a second time.

Once both cleaned scans were available, an attempt was made to align them using the automatic best-fit alignment method. However, due to insufficient overlap or surface complexity, this method failed to produce a correct result. To overcome this, the software's manual alignment feature was used, which allows the selection of up to five corresponding points between the two scans. These user-defined reference points served as a basis for the alignment, enabling the software to successfully register the scans and merge them into a coherent and continuous point cloud.

The best-fit alignment method employs an iterative closest point algorithm, minimizes the squared distances between overlapping scan points, thereby achieving a seamless integration of the different scans into a single mesh.

After merging the individual scans into a single point cloud within VXelements, the dataset was exported to VXmodel for more advanced mesh processing. In this environment, dedicated tools were used to correct potential mesh defects such as irregularities, spikes, and holes. Once all scans were successfully merged into a continuous mesh, a global cleaning operation was performed to remove any extraneous points that did not belong to the blade geometry, including data captured unintentionally from the rotating table. To address incomplete areas resulting from scanning limitations, the Fill Holes command was applied to reconstruct missing regions and generate a closed surface. This refined and watertight mesh served as a reliable foundation for developing the CAD model of the blade.

## 6.1. SCANNING PROCESS OF THE COMPRESSOR BLADE

---

During the initial scanning attempts, several issues were encountered that impacted the completeness and efficiency of the process. Firstly, the operator was not given clear guidance on which surfaces of the blade were most critical to capture. As a result, the focus was placed predominantly on the airfoil region, while the platform areas were not sufficiently covered. This led to missing sections in the platform, which had to be reconstructed artificially during mesh processing in the post-scan phase. One specific issue occurred during the scan of the sixth stage blade, where a non-functional surface was not properly captured. This was due to limited visibility in the two scanning orientations used in the initial setup, resulting in missing data in that region, as shown in Figure 6.3 with a red mark. Additionally, the highly reflective surface of the blade posed significant challenges for the scanner, especially in capturing fine details on certain faces. The fixed nature of the scanning table also introduced limitations, as the operator had to move around the part manually, often with constrained access and suboptimal scanning angles. In some cases, fine particles such as talcum powder can be applied to reduce reflections and improve scan quality, although this method was not used in the present process.

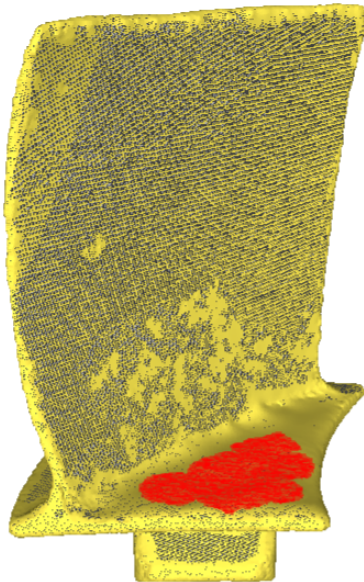


Figure 6.3: Missing surface area in the sixth stage blade scan.

In light of these difficulties, a change in the scanning strategy was implemented. A new setup was introduced using a rotative table with integrated targets, allowing the blade to be rotated smoothly while the scanner remained in a stable position, as shown in Figure 6.4. This change improved both the fluidity of the scan and the consistency of surface acquisition.

Setup  
Final

Figure 6.4: Final scanning setup with rotative table and integrated targets.

Furthermore, the number of scanning stages was increased from two to three, allowing for more thorough coverage of the entire blade geometry and ensuring that critical areas, such as the platform, were adequately captured. To specifically address the missing surface in the sixth stage blade, the third scanning position was performed with the blade placed vertically on the table surface, improving visibility and ensuring full data acquisition in that region. The three scanning positions used in this final configuration are illustrated in Figure 6.5.

Pos. Pos  
Final

Figure 6.5: Final three blade positions used in the revised scanning approach.

Finally, it should be noted that the leading and trailing edges of the blade exhibit several irregularities in the resulting mesh, as shown in Figure 6.6. Due to the extremely thin geometry of these regions, the scan resolution did not produce a sufficiently dense set of points to represent them smoothly, resulting in a jagged and discontinuous appearance. Although these edges are relevant to the scope of this work, the observed irregularities do not critically affect the overall objectives. This limitation will be addressed and corrected in the following chapter, where the CAD reconstruction process is detailed.

### 6.1. SCANNING PROCESS OF THE COMPRESSOR BLADE

---

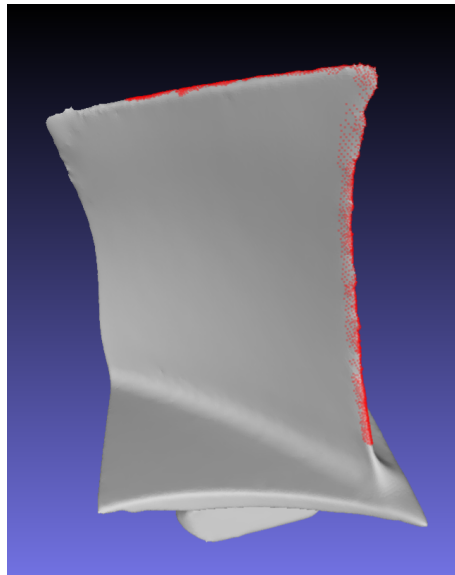


Figure 6.6: Irregularities in the leading and trailing edges of the scanned mesh caused by limited point density.

In summary, the scanning process for the compressor blade involved multiple orientations, manual alignment using best-fit techniques, and detailed mesh refinement to obtain a high-quality digital representation. Despite some limitations and challenges, the resulting scans provided a robust and accurate basis for subsequent CAD modeling and geometric analysis. Figure 6.7 shows the point cloud obtained from the scanning of the sixth stage blade.

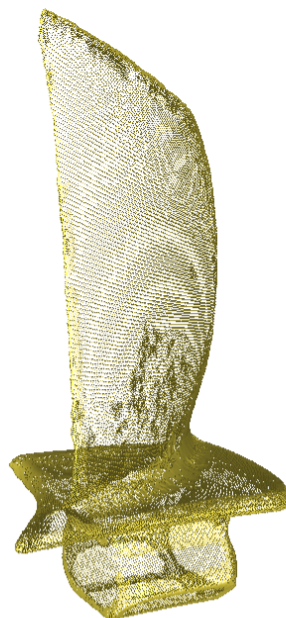


Figure 6.7: Stage 6 Point Cloud

## 6.2 Point Cloud Processing and CAD Model Creation

To generate the CAD model from the scanned data, the point cloud was processed and imported into SolidWorks using the Xtract3D add-in. This tool facilitated working directly with the point cloud by enabling reference geometry creation and surface sculpting based on the scanned data.

Unlike traditional workflows where an STL file is imported as a surface body to optimize processing, Xtract3D allowed for direct manipulation of the point cloud without losing critical geometric information. This streamlined the modeling process, reducing the need for intermediate conversions and preserving the fidelity of the scanned data.

Using the Xtract3D slice feature, cross-sections were extracted from the point cloud, as represented in Figure 6.8. This allows guiding the creation of accurate profiles and lofted surfaces that replicated the original blade geometry with high precision. By leveraging these tools, the CAD model was refined iteratively to match the scanned data while ensuring manufacturability and compatibility with further analysis.

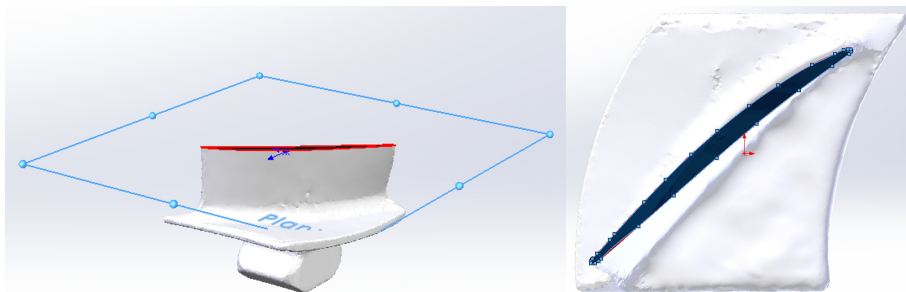


Figure 6.8: Mesh and CAD Comparison

As illustrated in Figure 6.9, this process enables the generation of an accurate CAD model from the scanned data.



Figure 6.9: Mesh and CAD Comparison

In the next section, the accuracy of the generated model will be evaluated against the scanned blade, accompanied by additional analyses, in order to ensure a parametric

---

## 6.2. POINT CLOUD PROCESSING AND CAD MODEL CREATION

model accurate enough to support the development of this dissertation.

# Design and Application of Tooling for CMM: Fixation System Modeling

In this chapter, the work previously developed by Farinha [5] will be reviewed, as it provided the foundation for the fixation system design. The fixture development presented here focuses exclusively on the blades of stages 6 and 7, with the understanding that the same design logic can be extended to stages 8, 9, and 10, requiring only geometric adaptations to accommodate the different dovetail profiles. The analyses and calculations carried out throughout the development of the prototype will also be discussed, offering insight into the technical decisions, constraints, and challenges encountered during the design process.

## 7.1 Past Work

The design of the fixture developed in this project was guided by principles outlined by Farinha (2021), particularly those related to the functional and geometric requirements of mechanical assemblies. A fixture must ensure the complete restriction of the six degrees of freedom of the workpiece, provide stable and repeatable positioning, and allow for efficient loading and clamping without compromising accuracy. Although the author does not explicitly refer to the 3-2-1 principle, the approach described is clearly aligned with it, aiming for robust constraint through strategically positioned contact points.

Another key consideration drawn from Farinha's work is the distinction between the locating elements, which ensure the correct positioning of the part, and the clamping elements, which apply the necessary forces to hold it during machining. The fixture must also be compatible with the specific operations required—namely milling—and with the expected geometric tolerances, avoiding distortions or positioning errors that could affect the final part.

These concepts formed the basis for the fixture proposed in this work, which was tailored to the particular geometry of the component, the machining constraints, and the overall manufacturing objectives.

## 7.2 Fixture Design

### 7.2.1 6th and 7th Stage Blade Geometry Assessment

Instead of designing a dedicated fixture for each stage, it was verified that the dovetail geometries of the blades from the 6th and 7th stages are sufficiently similar to allow the use of a single fixture for both. Figure 7.1 shows the overlap between the dovetails of a 6th stage blade (dark brown) and a 7th stage blade (beige), confirming the geometric compatibility. As a result, a single fixture will be designed to accommodate both stages.



Figure 7.1: Overlay of dovetail profiles from the 6th stage and 7th stage blades.

### 7.2.2 Blade Fastening System

The fixture was developed to constrain the HPC blade in the Y and Z directions through contact with two precisely machined blocks, both shaped to match the geometry of the blade's dovetail. This configuration ensures consistent vertical and lateral positioning, as illustrated in Figure 7.2, which presents an exploded view of the main components.

The top contact block interfaces with defined regions on the blade. These surfaces were selected to avoid functional zones while still providing the necessary mechanical stability. Figure 7.3 shows the contact areas on the blade itself, and Figure 7.4 highlights the corresponding surfaces on the fixture.

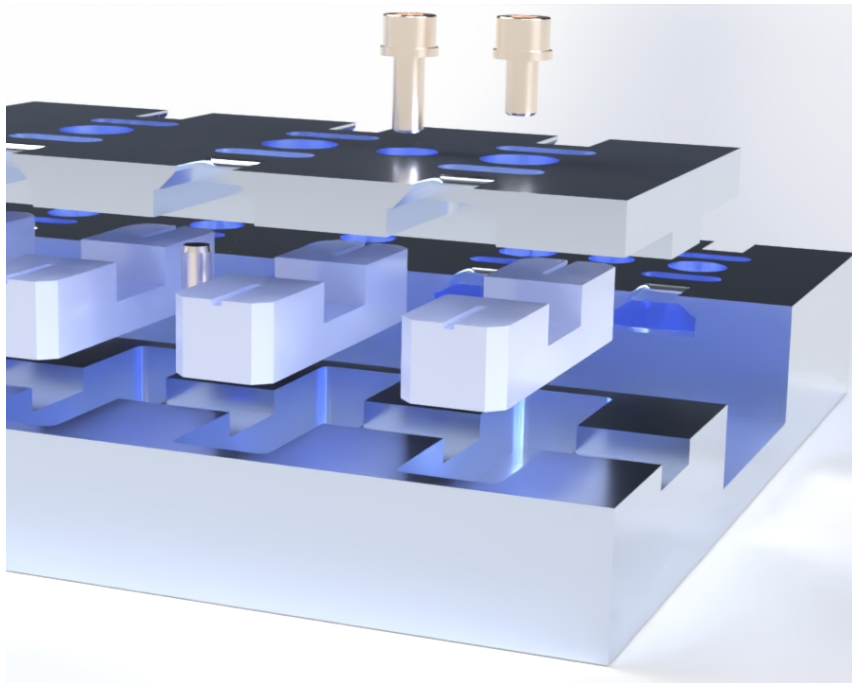


Figure 7.2: Exploded view of the fixture showing the base plate, bottom support block, top contact block, and clamping element. The geometry of the contact surfaces is adapted to the blade's platform and dovetail profile.

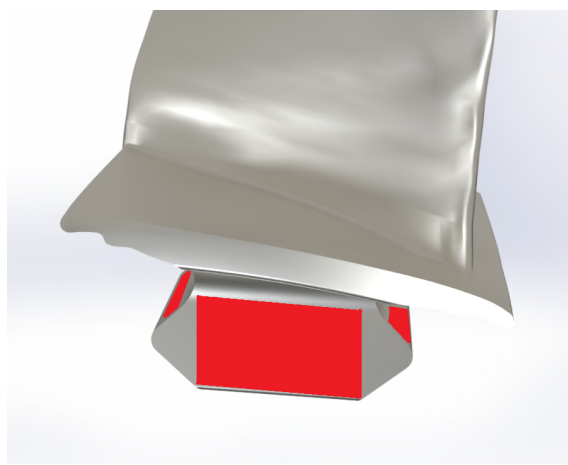


Figure 7.3: Contact surfaces on the blade that interface with the top contact block of the fixture.

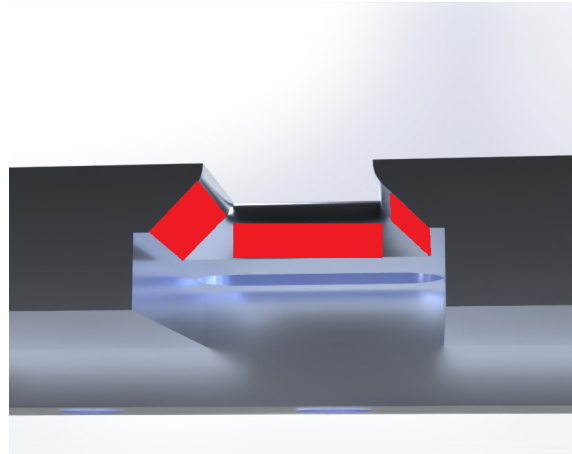


Figure 7.4: Contact surfaces on the top contact block of the fixture, matching the geometry of the blade.

Although the blade is not geometrically constrained along the X axis, a clamping element actuated by a screw applies a downward force that securely locks the blade in place. This pressure piece ensures immobilization during the measurement process. Small variations in the X position between blades are absorbed during the CMM alignment stage, since the coordinate system is redefined based on the actual part position before each measurement.

To prevent potential blade slippage during probing, a solution previously proposed and validated by Farinha (2021) was directly applied. In his prototype, it was observed that the combination of polished aluminium and titanium resulted in low friction, allowing the blade to move under small applied forces. To overcome this, Farinha recommended the use of a thin rubber strip at the contact surfaces. This increases the local friction coefficient and eliminates the need for high clamping forces. Given its proven effectiveness and its common use in MRO procedures, this solution was incorporated into the present fixture design by applying the rubber only on the relevant angular surfaces of the top contact block that interface with the blade.

### 7.2.3 Blade Spacing

### 7.2.4 Fixture Threading and Transportation Features

### 7.2.5 Fastening Feature of the Fixture with CMM's TTable

# Tool Design for Blade Clearance Control

Following the conclusions drawn in Section 5.1.4 regarding the actual contact points between blade platforms, this chapter focuses on applying reverse engineering to determine the chord length of the blade platforms and . The approach involves analyzing the contact zones identified previously and determine the correct platform chord dimensions. Furthermore, the diameters of the spool will be determined by opening a case with the manufacturer to request these specific dimensions, ensuring accuracy in the assembly process.

With this information, the chapter proceeds to the design of a tool for blade clearance control, capable of assessing the contact clearance between the blades during assembly. The tool will be designed based on nominal tolerances, estimated blade configurations, and the dimensional analysis of the spool diameter, ensuring precise control over the final assembly clearance.

## 8.1 Statistical Analysis for Tolerance Estimation

The first step in this process is determining how many blades need to be measured in order to obtain a credible and accurate chord dimension. To assess this, a statistical methodology was applied. Since no manufacturing tolerances were provided, these were estimated based on direct measurements performed with a caliper. The approach is grounded in standard principles of statistical quality control and process capability analysis, as detailed in Requeijo and Pereira's work on process planning and statistical control.

### 8.1.1 Sampling Strategy

Building upon the methodology, the next step is to determine the number of blades to be measured from each stage to ensure reliable results. A pilot sample was used to estimate the required number of measurements for process characterization. Six used blades were measured per stage using a digital caliper. The results for stages 6 to 10 are presented in Table 8.1. As shown in Figure 8.1, the dimension "x" represents the chord length being measured on the blade platform.

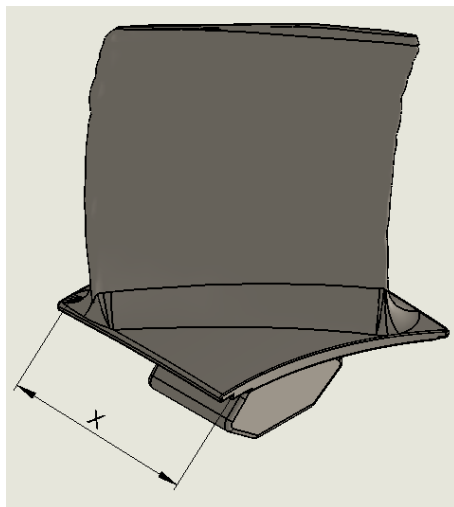


Figure 8.1: Platform blade with the chord dimension being measured, indicated as "x".

Table 8.1: Pilot measurements of platform chord lengths (mm) for stages 6 to 10.

<b>Stg 6</b>	<b>Stg 7</b>	<b>Stg 8</b>	<b>Stg 9</b>	<b>Stg 10</b>
18.71	20.37	18.59	19.48	18.26
18.71	20.36	18.58	19.49	18.28
18.72	20.37	18.61	19.46	18.28
18.72	20.36	18.58	19.47	18.26
18.71	20.36	18.59	19.48	18.28
18.72	20.37	18.57	19.48	18.28

Using this data, the required sample size  $n$  for a given confidence level of and measurement precision was determined using the expression:

$$n = \left( \frac{Z \cdot s}{E} \right)^2$$

Where:

- $Z$ : standard normal value for the chosen confidence level (in this case 1.96 for 95% of confidence),
- $s$ : standard deviation estimated from the pilot sample,
- $E$ : maximum acceptable error (typically set to 0.01 mm, matching the caliper's resolution).

The values of  $s$  and the corresponding sample sizes for each stage are presented in Table 8.2 for the narrow body type blades and on Table 8.3 for the wide body type blades.

Table 8.2: Calculated sample sizes for Narrow Body blades based on standard deviation from pilot sample, confidence level, and maximum error.

s	Z	E	n
0.006956076	1.96	0.005	7
0.006956076	1.96	0.005	7
0.013319872	1.96	0.005	27
0.013116504	1.96	0.005	26
0.006558252	1.96	0.005	7

Table 8.3: Calculated sample sizes for Wide Body blades based on standard deviation from pilot sample, confidence level, and maximum error.

s	Z	E	n
0.006956076	1.96	0.005	7
0.006956076	1.96	0.005	7
0.016558774	1.96	0.005	42
0.010625582	1.96	0.005	17
0.005679613	1.96	0.005	5

Regarding the number of measurements per blade, only one measurement was taken per blade. This choice is justified by the high resolution of the caliper, which is calibrated, and the repeatability of the measurement procedure, with measurements consistently performed by a single operator. According to principles described in the literature, and particularly by Requeijo and Pereira, when the measurement system is precise and the method is consistent, a single measurement per part is acceptable in statistical process control. Repeated measurements are mostly recommended when evaluating the measurement system itself (e.g., during a repeatability and reproducibility study).

### 8.1.2 Estimating Process Tolerance

Knowing the number of measurements needed per stage, the following step is measuring new HPC blades available on TAP's engine shop. For each blade group, the sample mean  $\bar{x}$  and standard deviation  $s$  were computed. Assuming normality in the data distribution, the process tolerance can estimated as:

$$T = 6s$$

According to literature this range is expected to encompass approximately 99.73% of blades, reflecting a standard tolerance interval associated with normally distributed processes.

Example for wide blades from stage 7:

- Measurements: {20.62, 20.62, 20.61, 20.62, 20.62, 20.62, 20.61} mm
- Mean:  $\bar{x} = 20.6171$  mm

- Standard deviation:  $s = 0.00488 \text{ mm}$
- Tolerance estimate:  $T = 0.02928 \text{ mm}$

Tables 8.4 and 8.5 present all the measurement results and estimated tolerances for each stage.

Table 8.4: Sample mean and tolerance estimates for each stage of the Narrow Body blades.

Stage	Narrow Body		
	Mean ( $\bar{x}$ )	Standard Deviation ( $s$ )	Tolerance Estimate ( $T = 6s$ )
6			
7	20.374	0.005345	0.032
8	18.591	0.007863	0.047
9	19.490	0.006939	0.042
10	18.284	0.005345	0.032

Table 8.5: Sample mean and tolerance estimates for each stage of the Wide body blades.

Stage	Wide Body		
	Mean ( $\bar{x}$ )	Standard Deviation ( $s$ )	Tolerance Estimate ( $T = 6s$ )
6	18.984	0.00535	0.032
7	20.617	0.00488	0.029
8	18.846	0.0059	0.035
9	19.753	0.00488	0.029
10	18.534	0.00548	0.033

As discussed in Section 5.1.1, the tolerance allowed for each blade at each stage, as shown in Table 5.1.1.1, is always larger than the tolerance estimated in this chapter, making it a solid and admissible estimation. Thus, it can also be concluded that the nominal chord length of the blade platform corresponds to the mean value presented in the tables.

Considering the mass production of these blades, and as previously mentioned, these tolerances must be analyzed through the statistical method. This approach assumes that the measurements of a specific dimension within a batch of parts follow a normal distribution. By analyzing, for example, an engine assembled in the workshop, and considering the number of wide, narrow, and lock blades per stage, it is possible to assess the potential dimensional variation of the blade set. The number of blades assembled per stage, as shown in Table 8.6, provides a clear overview of the blade distribution, which is essential for understanding the dimensional variability in the assembly process.

Table 8.6: Number of Wide, Narrow, and Lock Blades per Stage

Stage	Wide Blades	Narrow Blades	Lock Blades
Stg 6	36	22	4
Stg 7	33	20	4
Stg 8	39	20	4
Stg 9	37	19	4
Stg 10	38	22	4

$$\text{TolC} = \sqrt{T_N^2 \cdot (N + L) + T_W^2 \cdot W} \quad (8.1)$$

Where:

- $T_N$  is the tolerance associated with both narrow and lock blades (same value).
- $N$  is the number of narrow blades.
- $L$  is the number of lock blades.
- $T_W$  is the tolerance associated with wide blades.
- $W$  is the number of wide blades.
- TolC represents the total combined tolerance, taking into account the individual tolerances of both narrow and wide blades, as well as the number of blades of each type.

Applying equation 8.1.2, it is possible to evaluate whether the total dimensional variation at each stage remains within acceptable limits for the assembly process. Table 8.7 presents the calculated dimensional variation for each stage, showing a significant deviation in Stage 6, followed by substantially lower and consistent values in the subsequent stages, suggesting a stable manufacturing process.

Table 8.7: Total dimensional variation per stage

Stage	Dimensional Variation
Stg 6	
Stg 7	0.239
Stg 8	0.263
Stg 9	0.237
Stg 10	0.268

### 8.1.3 Conversion from Chord to Arc

Before defining the dimensions of the blade clearance control tool, it is essential to convert the measured platform chord length into the corresponding arc length, as the actual contact between the blades occurs along the circumference of the engine's spool perimeter.

Assuming a circular geometry, the relation between the chord  $c$ , arc length  $a$ , and radius  $R$  is given by:

$$a = R \cdot \theta = 2R \cdot \arcsin\left(\frac{c}{2R}\right)$$

Where:

- $c$ : chord length of the platform,
- $R$ : radius of the stage perimeter,
- $a$ : arc length corresponding to that chord.

In practice, for small angles and short chords the chord and arc are approximately equal. However, to ensure dimensional precision in the tool design, the arc length is computed using the actual measured chord and known stage radius.

Table 8.8: Chord and Tolerance for Each Stage (Wide and Narrow)

Stage	Wide		Narrow	
	Arc length (mm)	Tolerance (mm)	Arc length (mm)	Tolerance (mm)
6	20.383	0.032	18.992	0.032
7	20.383	0.032	20.626	0.029
8	18.598	0.030	18.853	0.031
9	19.498	0.030	19.761	0.029
10	18.291	0.032	18.541	0.033

#### 8.1.4 Spool diameter Tolerancing

In order to accurately define the measurement process of the blade platforms, it is also essential to consider the potential dimensional variation of the spool on which the blades are mounted. Since this component is not readily available in large quantities at the TAP engine maintenance facility, only two spools were available throughout the course of this dissertation. The measurements were taken on the blade platform side of the spool, specifically in the region where blade-to-blade contact occurs, as illustrated in Figure 5.3 and referred to as the Diameter Up.

Table 8.9: Spool measurements for engines 418 and 463

in		mm	
418	463	418	463
15.550	15.550	394.970	394.970
15.615	15.615	396.621	396.621
15.677	15.677	398.1958	398.1958
15.704	15.705	398.8816	398.9070
15.690	15.688	398.5260	398.4752

Given that only two components were available, it was not possible to carry out a statistical analysis similar to the one performed for the blades. As such, a fundamental tolerance grade was assumed to define the dimensional variation of the spool, based on tolerances applied to diameter-related dimensions in other critical components.

For example, in the case of the LPT shaft, although the exact manufacturing dimensions are not available, the operational limits provided by the manufacturer are known. For this part, the inner diameters have an operational tolerance of 0.004 mm, which implies that the manufacturing tolerance must be even tighter to ensure the part remains functional under operating conditions. Assuming a safety factor of 2, a manufacturing tolerance of 0.002 mm can be considered reasonable.

By consulting the table of fundamental tolerances and noting that this diameter falls within the range of 180 mm to 250 mm, it corresponds to an IT01 grade, the tightest standard tolerance for that size range. This demonstrates the high level of manufacturing precision achievable by the supplier.

Taking this into account, it is reasonable to adopt an IT grade for the spool diameter in order to address the dimensional variation in the absence of a sufficiently large sample size. By assuming an IT3 classification, which is considerably less strict than the tolerance estimated for the LPT shaft, the spool diameters can be associated with a manufacturing tolerance of approximately 0.013 mm.

The corresponding nominal dimensions and assumed tolerances are presented in Table 8.10.

Table 8.10: Nominal spool diameters and assumed manufacturing tolerance (IT3)

Nominal Diameter [mm]	Tolerance [mm]
394.970	±0.0065
396.621	±0.0065
398.1958	±0.0065
398.8816	±0.0065
398.5260	±0.0065

## 8.2 Tool Design

Building on the conclusions drawn from the statistical analysis of the blade platforms in the previous section, this chapter addresses the design of a tool for controlling blade clearance. The primary objective of this tool is to measure the sum of the chord lengths of all blades per stage, facilitating the prediction of whether the assembled set meets the required clearance for optimal operation, in accordance with the established operational limits.

The design process will incorporate nominal tolerances, estimated blade configurations, and dimensional analysis of the spool diameter, guaranteeing accurate control over the final clearance during assembly.

### 8.2.1 Material

The aim of this section is to determine the material to be used for manufacturing the tool, which will be machined on a CNC machine. In order to make an informed decision, several factors must be considered, including cost, weight, and machinability.

The selection of aluminum for the tool is based on its superior machinability, reduced tool wear, and high-speed cutting capability compared to steels and other harder materials. Aluminum allows significantly higher cutting speeds while maintaining good dimensional accuracy and excellent surface finish. Its lower hardness, high thermal conductivity, and resistance to built-up edge formation make it ideal for processes where precision and surface integrity are critical. Furthermore, its widespread availability and compatibility with various surface treatments make it an economically efficient and technically versatile material for tooling applications [13].

Among the available aluminum alloys, the 6000 series is highlighted in the literature as offering a favorable balance between strength, corrosion resistance, and machinability. Specifically, alloy 6061 is identified as a reliable option due to its good mechanical properties and consistent cutting behavior, making it a suitable and well-established choice for both structural and precision-machined components [13].

Although PTFE (Teflon) was also considered as an alternative material, a comparison of the component weights shows that the aluminum version weighs 7168.82 grams, while the PTFE version weighs 6159.88 grams. The relatively small difference in mass demonstrates that the aluminum tool remains light enough to be easily handled and transported by the operator, while offering significantly better mechanical robustness and durability compared to PTFE.

## 8.3 Design Considerations

One of the key aspects to consider when defining the most suitable tool design is the geometry of the dovetail sections of the blades. Since the blades are secured to the tool via these dovetail interfaces, their dimensional characteristics play a critical role in ensuring a proper fit and functional engagement.

To characterize this geometry, ten blades were measured from each stage. For each blade, four key dimensions of the dovetail were recorded: A, B, C, and D. These correspond respectively to the upper width, lower width, total height, and lateral offset of the dovetail profile.

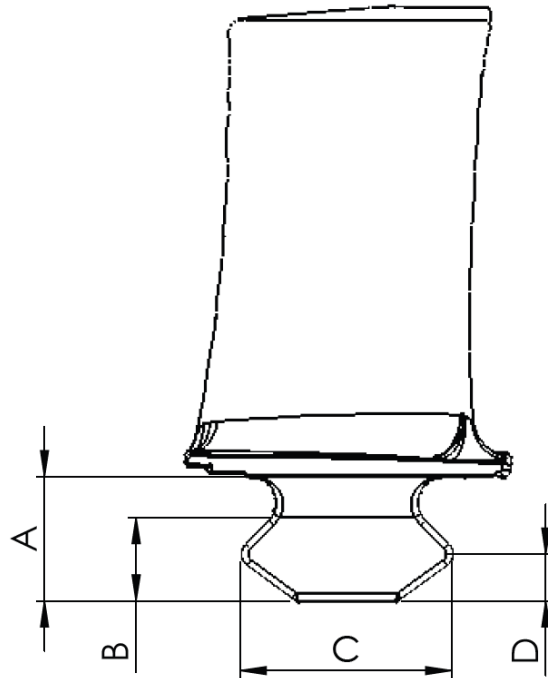


Figure 8.2: Schematic representation of the dovetail geometry and its key dimensions (A, B, C, D).

Figure 8.2 illustrates the progressive variation in dovetail geometry across different stages of the system. The dimensions labeled A, B, C, and D refer respectively to the upper width, lower width, height, and lateral offset of each dovetail segment.

Table 8.11 summarizes the measured values for each geometric parameter from stage 6 to stage 10. As observed, dimension A decreases consistently from 8.20 mm at stage 7 to 6.70 mm at stage 10, indicating a narrowing of the top surface. Similarly, dimension C (height) follows a downward trend, supporting a compact design. Dimension B and D exhibit more variability, potentially reflecting design adaptations for mechanical engagement or alignment tolerance.

Table 8.11: Dovetail dimensions across different stages

Stage	A (mm)	B (mm)	C (mm)	D (mm)
6	–	–	–	–
7	8.20	4.90	13.60	2.70
8	7.70	5.30	12.70	1.80
9	6.90	4.15	11.00	1.90
10	6.70	4.73	10.20	2.10

The engagement between the blade and the tool is defined by dimension C. Therefore, the fit between both parts must be carefully selected to ensure accurate chord measurements. The goal is to allow the blades to be inserted manually into the tool and to slide

along it with minimal resistance, while still limiting excessive clearance that could compromise the accuracy of the measurements. According to [17], for medium mechanical precision and a sliding fit, the recommended tolerances are H8 for the hole and h8 or h9 for the shaft.

In addition to the dovetail geometry, another critical consideration in the design of the tool is the definition of the operational limits for the sum of the blade chords within the slot. These limits are essential for establishing the acceptable dimensional range to be used during blade inspection and tool setup.

To define these operational limits, a combined reasoning approach was followed:

Firstly, the dimensional variation of the spool was considered. By analyzing the maximum and minimum values of the spool perimeter ( $P_{max}$  and  $P_{min}$ ) for each stage, and subtracting the maximum and minimum admissible clearances, a functional tolerance window was obtained. This defines the upper and lower bounds for the sum of blade chords to be accepted within the tool.

Secondly, it was necessary to account for the geometric transition from arc to chord. In the engine, blades are arranged along a circular arc, whereas in the tool, they are positioned linearly. Since the number of blades per stage is known, but not the exact combination of narrow, wide. This involved calculating the maximum total reduction between arc length and chord length across all blades in a stage, which was then subtracted from the spool perimeter to reflect the actual linear dimension that the chord sum must comply with.

Figure 8.3 illustrates this rationale, showing how the functional interval for the acceptable chord sum was derived by combining perimeter-based variation.

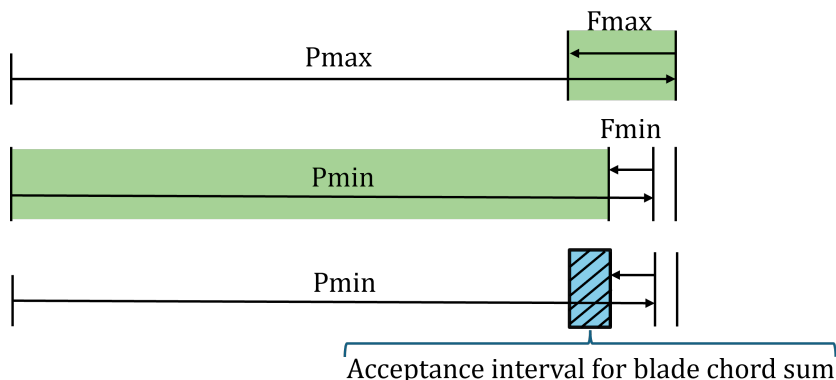


Figure 8.3: Functional tolerance window for the total blade chord length, based on spool perimeter limits adjusted by clearance allowances and arc-to-chord transformation.

Table 8.12 presents the final admissible limits obtained for each stage, considering both clearance requirements and arc-to-chord transformation effects.

Table 8.12: Admissible limits for the total blade chord length per stage

Stage	Min (mm)	Max (mm)
6	1244.030	1244.479
7	1249.135	1249.582
8	1254.176	1254.624
9	1254.548	1254.996
10	1251.619	1252.068

Based on all the considerations previously discussed, a first version of the tool was developed as a single-piece component.

The tolerances applied to the defined fit for the slots are shown in Figure 8.4, which provides an overall view of the tool. The detailed technical drawing of the slot is presented in Figure A.11.

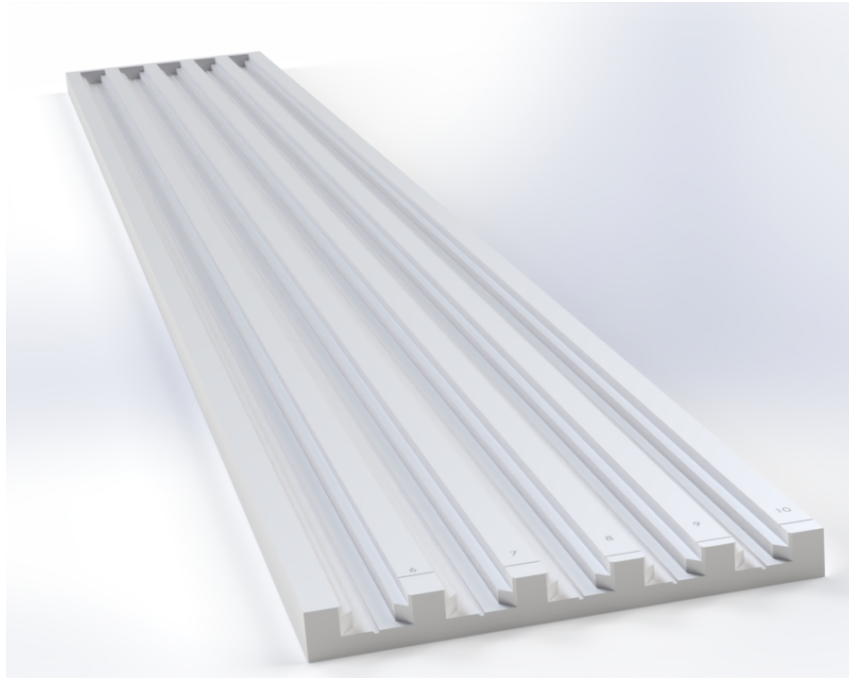


Figure 8.4: First Tool Design.

## 8.4 Prototype Manufacturing

Following the definition of the final geometry and tolerances for the tool, the next step involved the construction of a physical prototype. The aim was to validate the design assumptions and assess the feasibility of the manufacturing process, as well as the functionality of the tool in practical terms.

To initiate the validation phase, an initial prototype was produced using 3D printing in PLA. This 3D-printed model served primarily as a physical reference to analyse the fit and assembly of the blades within the tool body. It also allowed for a preliminary assessment of the channel geometry, helping to visualise its trajectory and anticipate

potential challenges during CNC machining, particularly in relation to tool accessibility and clearance.

Figure X presents the PLA prototype, while Figure Y illustrates the assembly of the blades onto the 3D-printed tool. This tangible analysis enabled the identification of critical areas requiring design adjustments to accommodate the constraints of the milling process.

Following this evaluation, a revised 2D technical drawing was produced, incorporating specific modifications under a design-for-manufacturing (DFM) approach. These changes included adjustments to the internal radii and geometrical simplifications, ensuring compatibility with standard end mill dimensions and improving the overall manufacturability of the component.

## Bibliography

- [1] K. Aainsqatsi. *Schematic Diagram of a 2-Spool, High-Bypass Turbofan Engine*. [Online; accessed 13-February-2025]. 2008-05. URL: [https://commons.wikimedia.org/wiki/File:Turbofan\\_operation.png](https://commons.wikimedia.org/wiki/File:Turbofan_operation.png) (cit. on p. 6).
- [2] *Brochure LEAP fiches 2017*. Brochure document. 2017 (cit. on pp. 6, 7).
- [3] A. Comercial. *Frota - TAP Air Portugal*. [Online; accessed 30-January-2025]. 2024-12. URL: <https://www.aviacaocomercial.net/frotatap.htm> (visited on 2024-12-01) (cit. on p. 3).
- [4] M. A. Engines. *LEAP-1A/-1B Commercial Aircraft Engines*. [Online; accessed 13-February-2025]. 2025. URL: <https://www.mtu.de/engines/commercial-aircraft-engines/narrowbody-and-regional-jets/leap-1a/-1b/> (cit. on p. 7).
- [5] E. E. Farinha and M. J. A. Santos. *Fixture Design and CMM Program Development for Measuring of High Pressure Compressor Rotor Blades*. Co-adviser: Mário Almeida Santos. 2021 (cit. on pp. 1, 22, 44).
- [6] B. Fehrm. *Björn's Corner: New engine development. Part 22: High turbine technologies*. [Online; accessed 13-February-2025]. 2024-08. URL: <https://leehamnews.com/2024/08/30/bjorns-corner-new-engine-development-part-22-high-turbine-technologies/> (cit. on p. 8).
- [7] R. R. A. Group. *The Jet Engine*. Fifth. Rolls-Royce plc, 2007. ISBN: 0902121235 (cit. on pp. 4, 5, 12, 14, 16).
- [8] A. C. D. S. Guerreiro. *Development of a Process to Measure the Exit Flow Area of the Low Pressure Turbine Nozzle from the CFM56-5B Engine*. Thesis or internal report. N/A (cit. on p. 22).
- [9] J. M. Lourenço. *The NOVAtesis L<sup>A</sup>T<sub>E</sub>X Template User's Manual*. NOVA University Lisbon. 2021. URL: <https://github.com/joaomlourenco/novathesis/raw/master/template.pdf> (cit. on p. ii).

- [10] S. Metals. *INCONEL 718 Alloy*. [Online; accessed 06-February-2025]. URL: <https://www.specialmetals.com/documents/technical-bulletins/inconel/inconel-alloy-718.pdf> (visited on 2025-02-06) (cit. on p. 16).
- [11] A. Mourão. *UNIVERSIDADE NOVA DE LISBOA FACULDADE DE CIÊNCIAS E TECNOLOGIA DEPARTAMENTO DE ENGENHARIA MECÂNICA E INDUSTRIAL MESTRADO INTEGRADO EM ENGENHARIA MECÂNICA DIMENSIONAMENTO FUNCIONAL E TECNOLÓGICO*. 2004 (cit. on p. 26).
- [12] T. A. Portugal. *Manual de Manutenção Oficial LEAP1A - Hardware*. 2020 (cit. on pp. 8–11, 13, 15–17).
- [13] M. M. Rahman et al. “Review of improvement of machinability and surface integrity in machining on aluminum alloys”. In: *Materials Today: Proceedings* (2023). DOI: [10.1016/j.matpr.2023.06.143](https://doi.org/10.1016/j.matpr.2023.06.143). URL: <https://doi.org/10.1016/j.matpr.2023.06.143> (cit. on p. 55).
- [14] P. Rendas. *Fixture Design and Process Development for High Pressure Compressor Rotor Blades Measuring in Aircraft Engine Maintenance*. 2021, pp. 1–45 (cit. on p. 22).
- [15] Renishaw. *Renishaw: Enhancing Efficiency in Manufacturing and Healthcare*. <https://www.renishaw.com/en/renishaw-enhancing-efficiency-in-manufacturing-and-healthcare--1030>. Accessed: 2025-02-13. 2025 (cit. on p. 21).
- [16] L. Shi et al. “A Review on Leading-Edge Erosion Morphology and Performance Degradation of Aero-Engine Fan and Compressor Blades”. In: *Energies* 16 (7 2023-04), p. 3068. ISSN: 1996-1073. doi: [10.3390/en16073068](https://doi.org/10.3390/en16073068) (cit. on pp. 18, 21).
- [17] *Tabela de Ajustes Mecânicos*. Documento interno. Consultado em 2025. Instituto Superior de Engenharia ou similar, s.d. (Cit. on p. 57).
- [18] Trent1. *Axial Compressor and Turbine Operation*. <https://www.phase-trans.msm.cam.ac.uk/mphil/Trent1/sld011.htm>. Accessed: 2025-02-13. n.d. (Cit. on p. 11).

# A

## Appendix

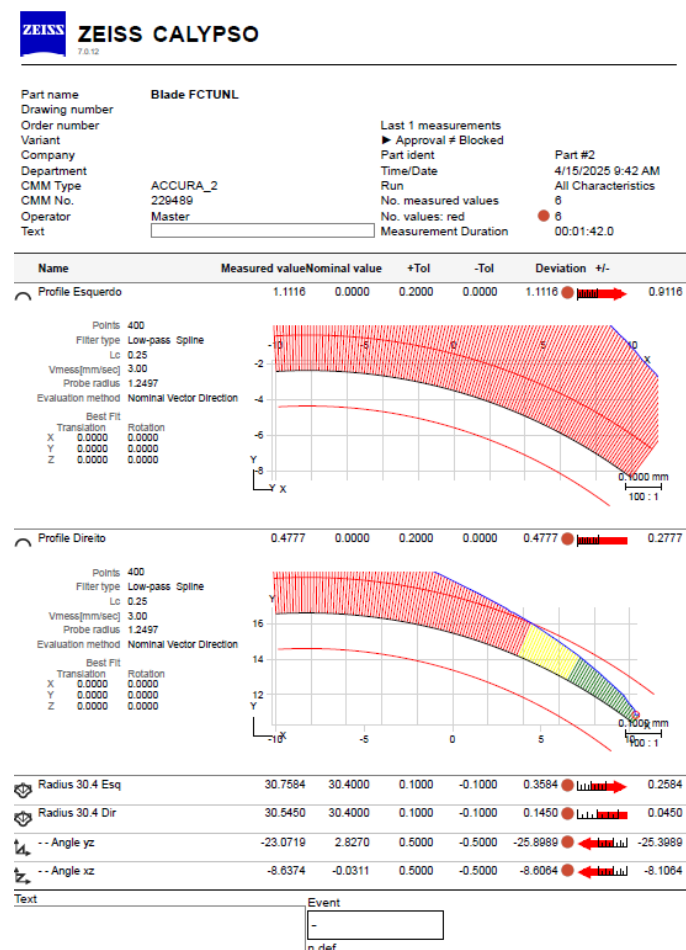


Figure A.1: Profile Measurement Report Blade 1

**ZEISS CALYPSO**

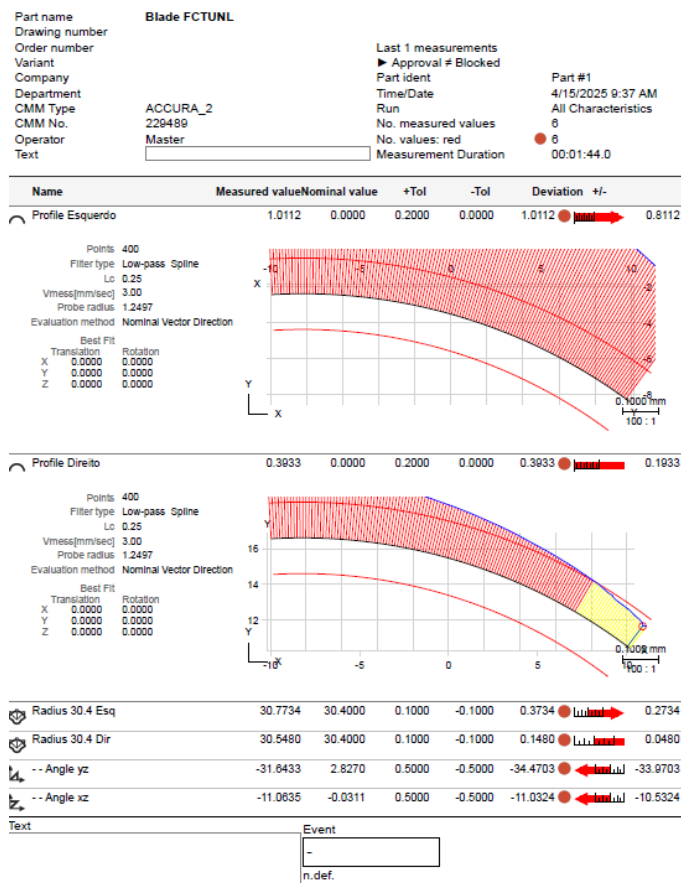


Figure A.2: Profile Measurement Report Blade 2

## APPENDIX A. APPENDIX

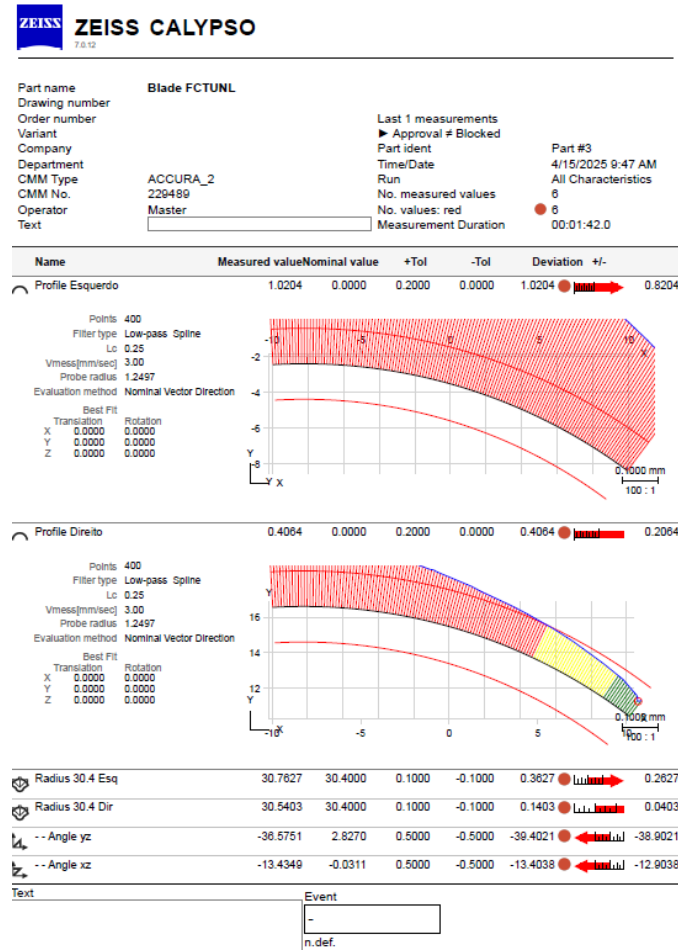


Figure A.3: Profile Measurement Report Blade 3

**ZEISS CALYPSO**

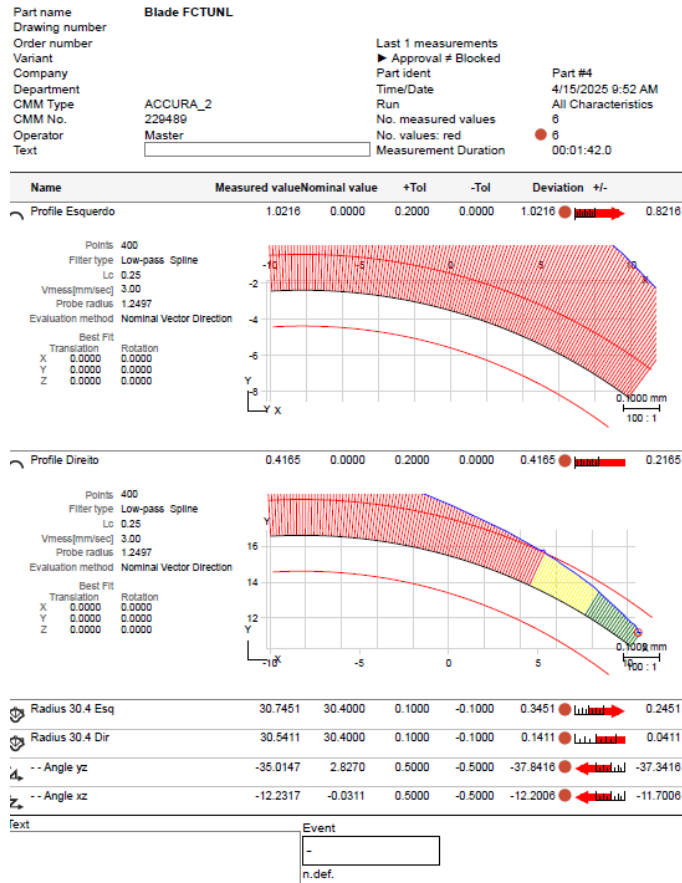


Figure A.4: Profile Measurement Report Blade 4

## APPENDIX A. APPENDIX

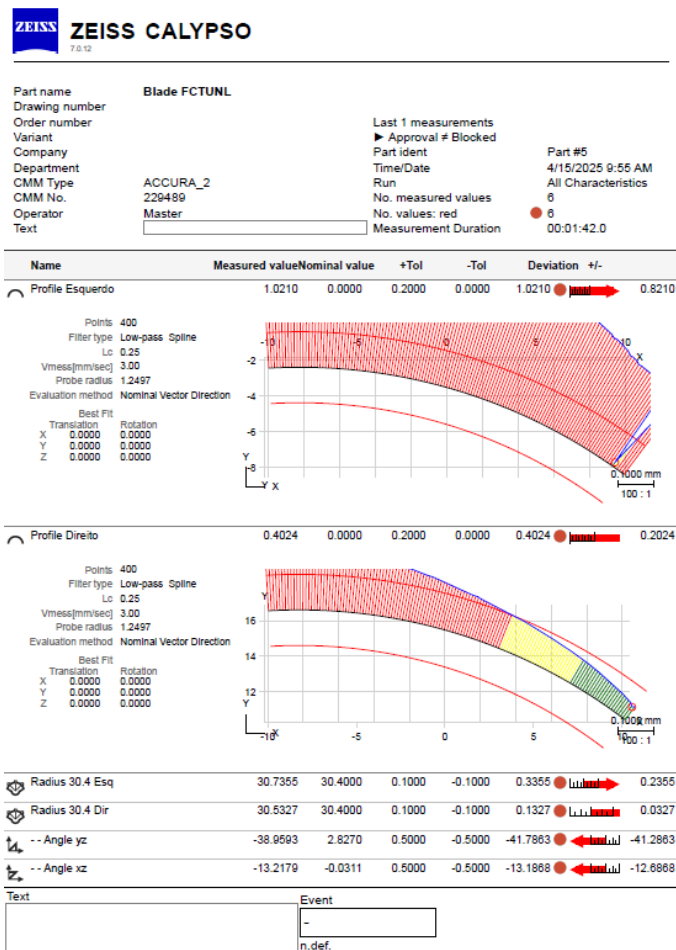


Figure A.5: Profile Measurement Report Blade 5

**ZEISS CALYPSO**

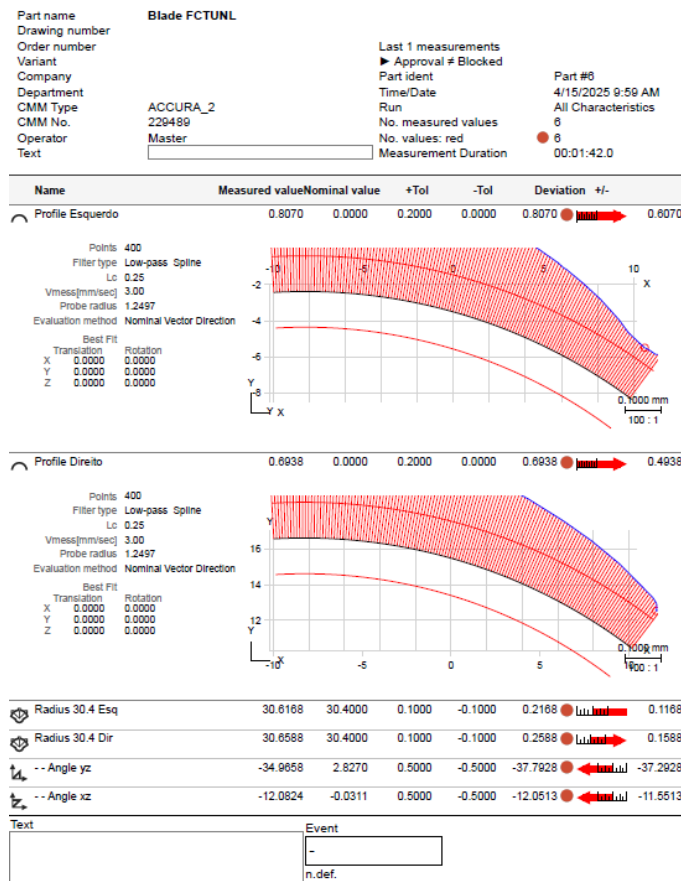


Figure A.6: Profile Measurement Report Blade 6

## APPENDIX A. APPENDIX

---

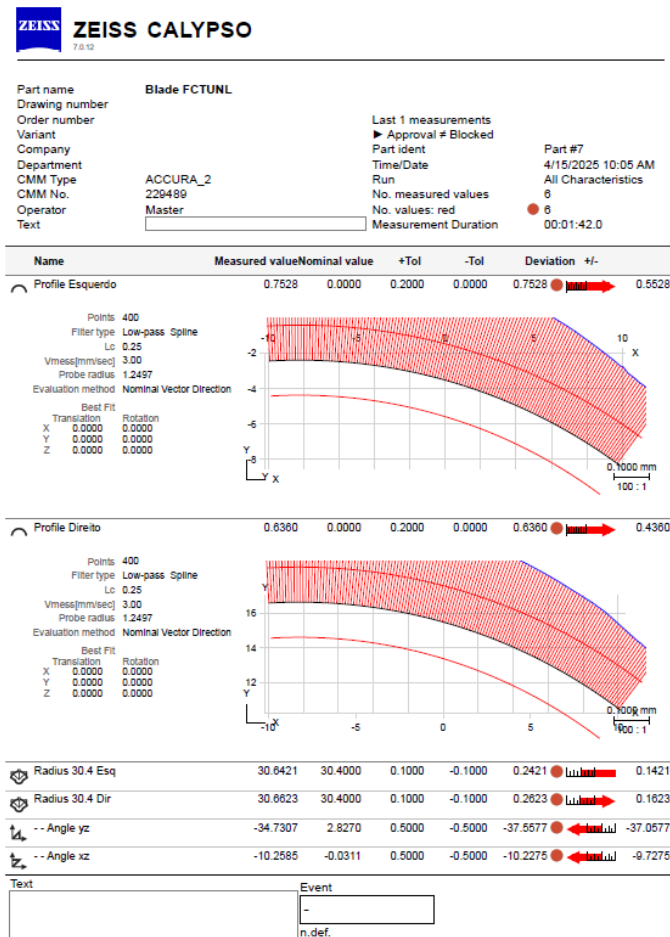


Figure A.7: Profile Measurement Report Blade 7

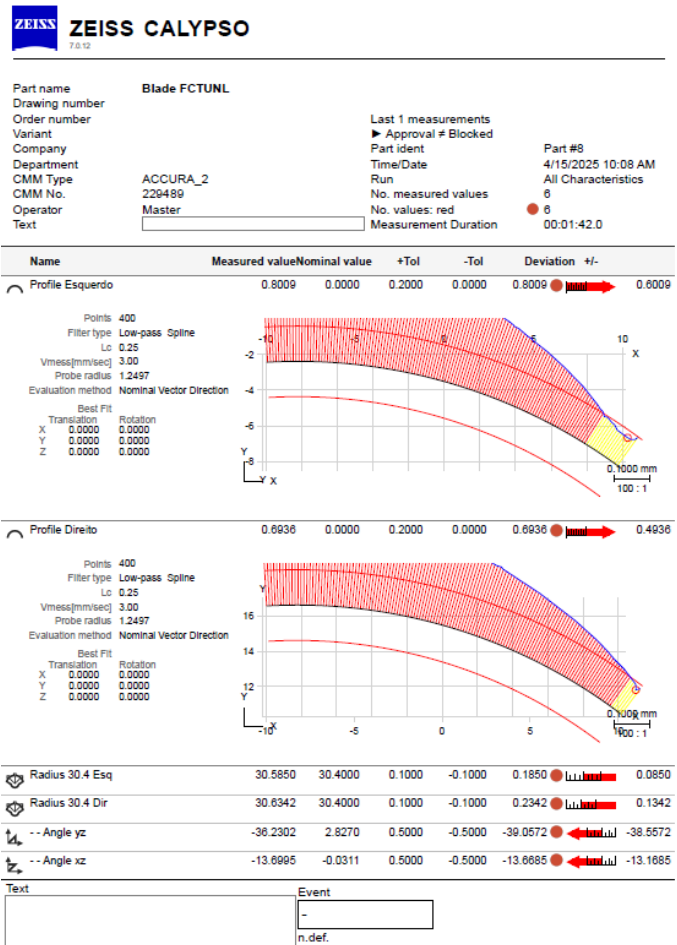


Figure A.8: Profile Measurement Report Blade 8

## APPENDIX A. APPENDIX

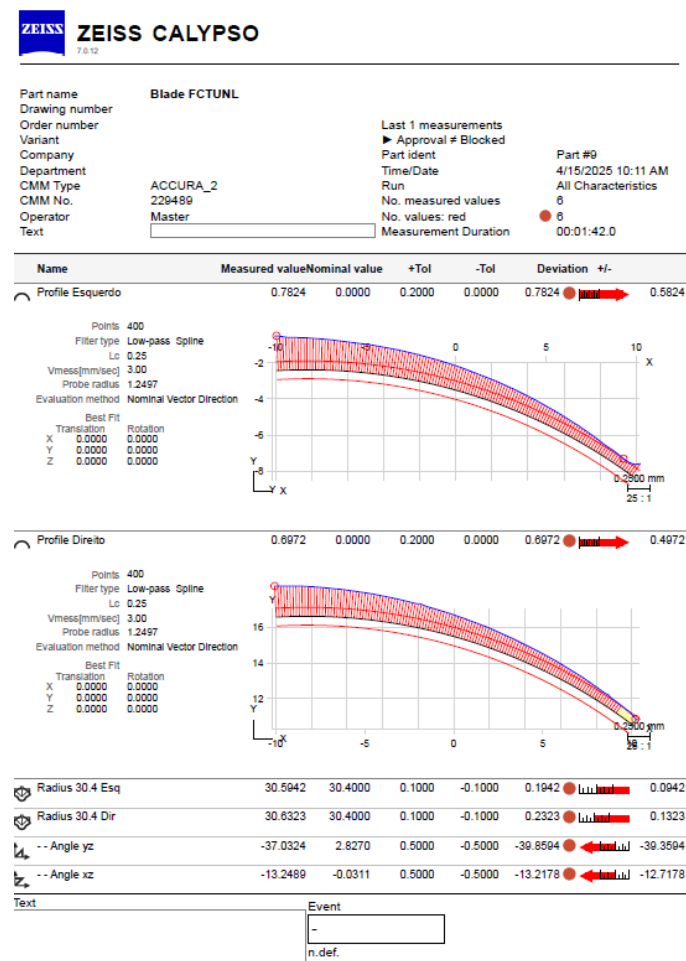


Figure A.9: Profile Measurement Report Blade 9

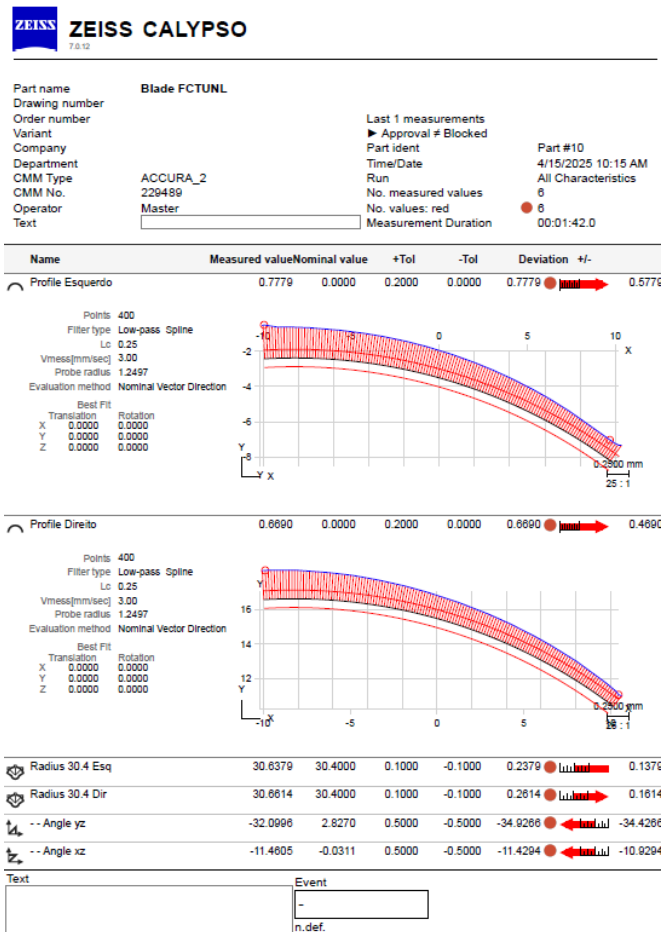


Figure A.10: Profile Measurement Report Blade 10

## APPENDIX A. APPENDIX

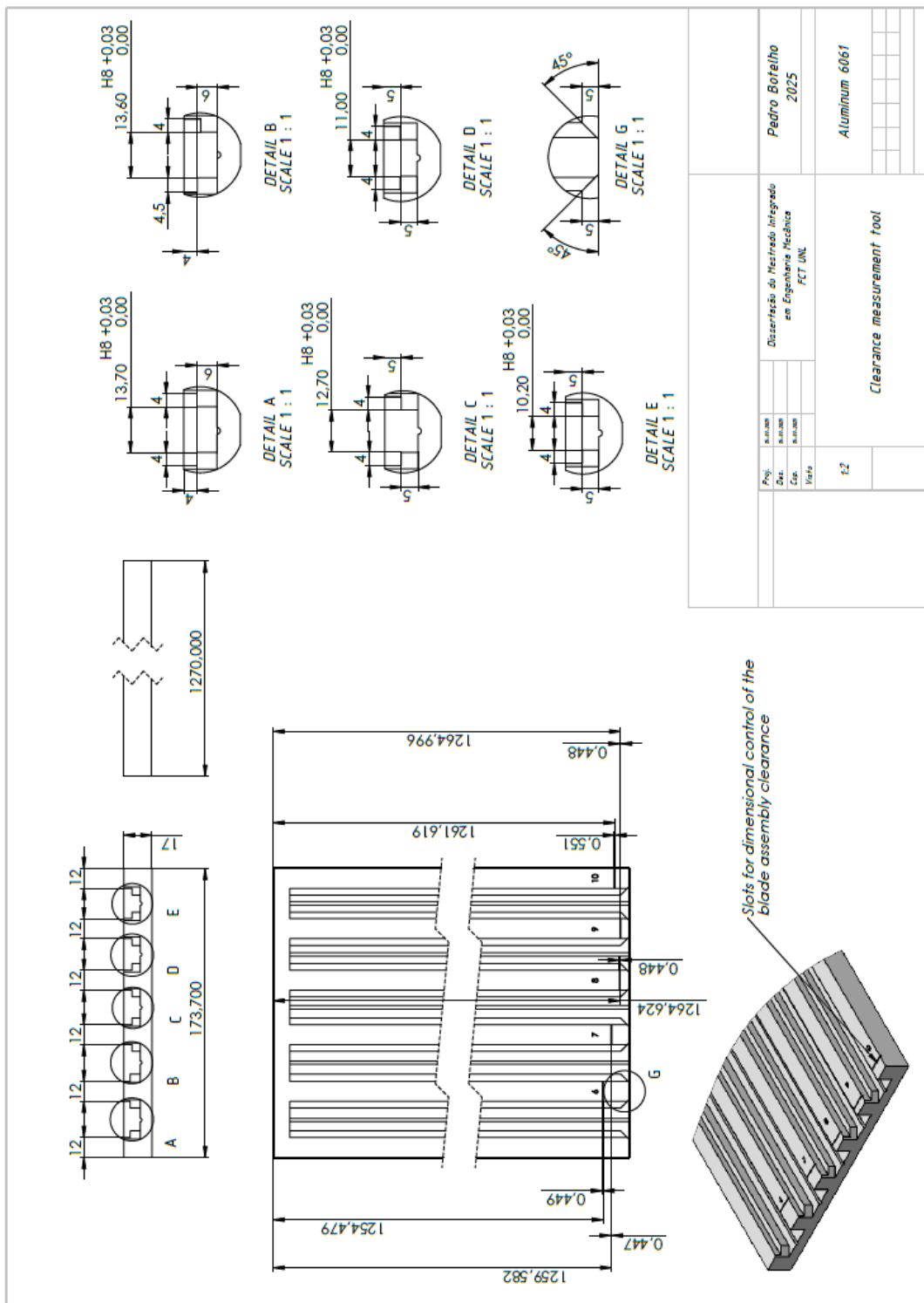


Figure A.11: First Tool Version 2D Drawing



